Super-Chandrasekhar-mass white dwarfs as Type Ia supernova candidates

R.C.J. Knaap

Supervisors: N. Langer & S.-C. Yoon

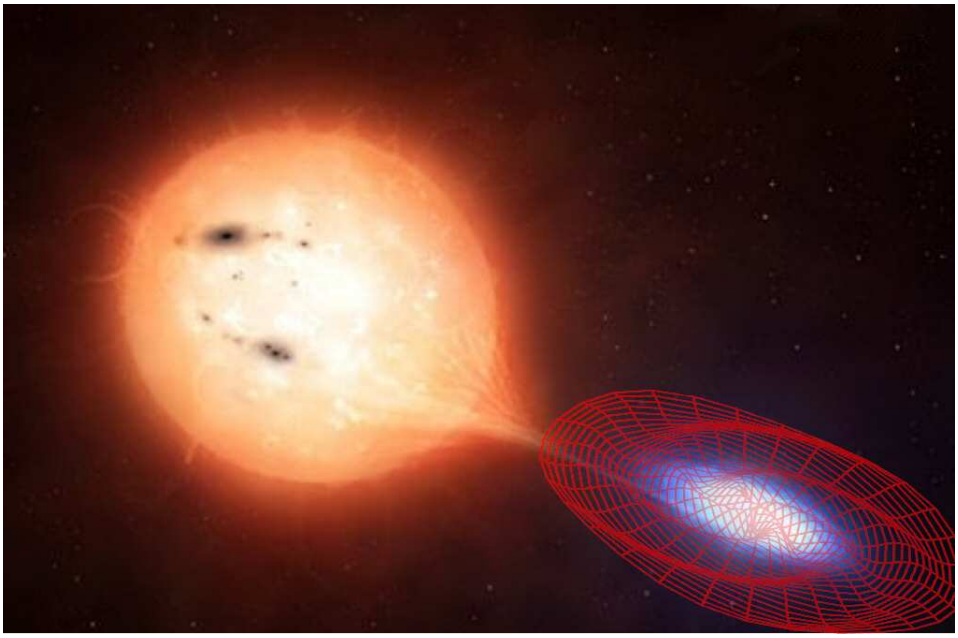

"The important thing is not to stop questioning. Curiosity has its own reason for existing." A. Einstein

Super-Chandrasekhar-mass white dwarfs as Type Ia supernova candidates

R.C.J. Knaap
Supervisors: N. Langer & S.-C. Yoon

Sterrekundig Instituut Utrecht

Universiteit Utrecht

November 2004

Contents

1 Introduction

Observations of nearby supernovae of Type Ia show that there exists a tight relation between the absolute peak brightness of these events and their luminosity decline rate (1, (Phillips, 1993)). This relation (called the Phillips relation) can be used to determine the absolute peak brightness of distant Ia supernovae of which only the apparent peak brightness and the luminosity decline rate can be measured and subsequently compute their luminosity distance (D_{L}), provided that the Phillips relation still holds for Type Ia supernovae at such high redshifts. If their redshift z can also be determined then the two can be combined to get an observational relation between D_{L} and z .

The theoretical relation between D_{L} and z is known and depends on a limited number of parameters, like the densities of matter and energy in the Universe (Ω_{M}, Ω_{Λ}) and the current Hubble constant (H_0). The value of some of these parameters can by found by fitting the theoretical to the observational relation between D_{L} and z (Perlmutter and Schmidt, 2003). Observations done by Knop et al. (2003) of Type Ia supernovae at high redshift (up to $z = 0.86$) strongly point to the existence of a Cosmological Constant. This method to determine Ω_{Λ} is an independent complement to the method based on measurements of the Cosmic Microwave Background radiation done by the satellite WMAP (Bennett et al., 2003).

So, Type Ia supernova observations allready help us understand the fabric of our Universe, but alas the event itself is not fully understood. What is certain from spectral observations however is that Type Ia supernovae are thermonuclear explosions of carbon-oxygen white dwarfs

The main thermonuclear explosion scenarios found in the literature are: sub-Chandrasekhar-mass carbon-ignition by helium detonation and the Chandrasekhar-mass double and single degenerate scenarios. In the sub-Chandrasekhar-mass scenario, a carbon-oxygen white dwarf orbits a non-degenerate star whose outer layers have swollen so much that mass is transfered from the non-degenerate star to the white dwarf (cf. Fig 2). The hydrogen that accretes onto the white dwarf burns quiescently to helium, forming a growing degenerate helium-layer. When the density at the bottom of the layer exceeds a critical value, the helium ignites and sends a strong shockwave inwards through the sub-Chandrasekhar-mass white dwarf (typically 1–1.1 $\mathrm{M}_{\odot}$). This shockwave converges at the centre of the white dwarf and ignites a detonation wave that disrupts the whole white dwarf (Woosley et al., 1986). The spectra produced by such events are however too blue to match the observations (Höflich et al., 1996).

The radius of white dwarfs decreases with increasing mass. In the case of carbon-oxygen white dwarfs this means that when they are above a certain mass the central density becomes high enough for carbon burning. The mass at which this happens lies close to the critical white dwarf mass, first calcu-

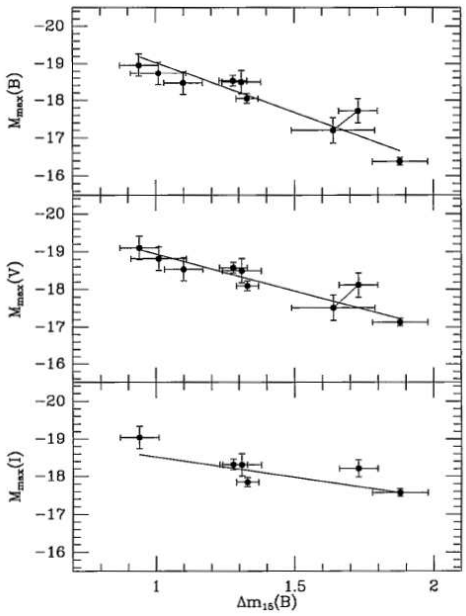

Figure 1: Phillips relation, linking the peak absolute brightness and luminosity decline rate of Type Ia supernovae. The vertical axis gives the peak luminosity in three colour bands and the horizontal axis the decline in luminosity after 15 days, for several observed Ia supernovae. From (Phillips, 1993).

lated by Chandrasekhar, above which the internal pressure is not enough to prevent gravitational collapse. This density-induced carbon ignition is the basis of the other two scenario's.

In the double degenerate scenario two sub-Chandrasekhar-mass white dwarfs form a compact binary. They merge due to orbital angular momentum loss through gravitational radiation and form one Chandrasekhar-mass white dwarf and a thick accretion disk. Modeling of these events by Saio and Nomoto (1998) suggests that because of the high mass accretion rate they do not lead to Type Ia supernovae but to neutron star formation due to electron capture.

This leaves us with the most probable scenario for Type Ia supernovae: the single degenerate core-ignition scenario (Livio, 2000). Here the binary system consists of a white dwarf and a non-degenerate companion. The mass transfered from the non-degenerate star to the white dwarf consists of hyrogen or helium, but this time the accretion rate is such that there is stable helium burning instead of helium flashes, so there are no shockwaves running trough the star. If angular momentum accretion is not taken into account, this scenario predicts that all the supernova Ia progenitors explode at the same mass of $\simeq 1.38\,\mathrm{M}_{\odot}$.

Although Branch et al. (1993) argue that so-called 'peculiar' Type Ia

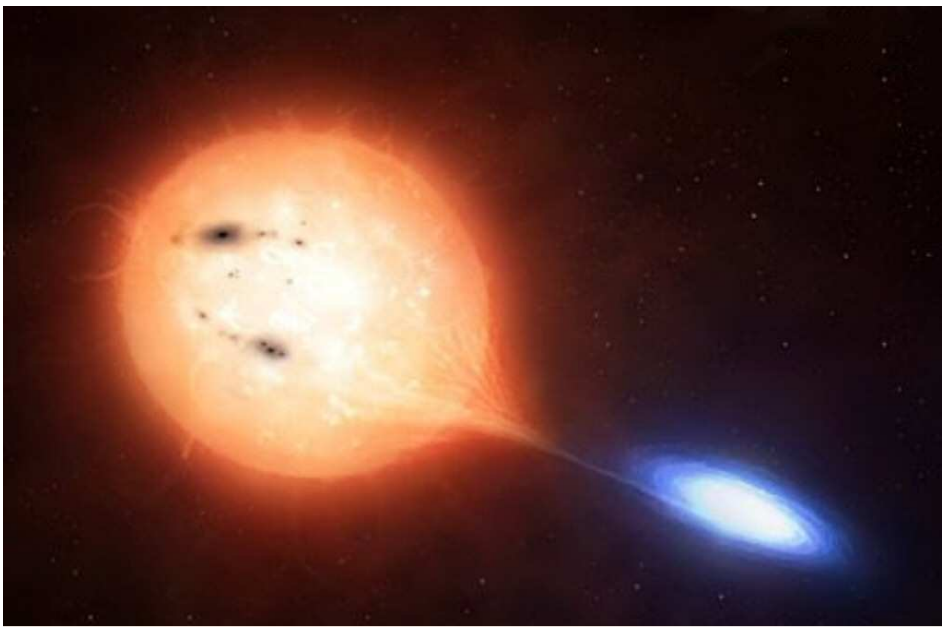

Figure 2: Artist's impression of a binary system containing a masstransfering main-sequence star and a white dwarf. The white dwarf itself is not visible because it is hidden within the (white) accretion disk. Image made by Mark A. Garlick.

supernovae are overrepresented in Fig. 1 and that the spread in peak luminosity of 'Branch normal' Type Ia supernovae is smaller, there remains a spread in peak luminosities and this is hard to explain when all ignition masses are identical. Explanations that have been suggested relate to different metalicities and different carbon-to-oxygen ratios. But the results of nummerical simulations done by Höflich et al (1998) and Röpke and Hillebrandt (2004) predict only small variations in brightness due to variations in the carbon-to-oxygen ratio and metalicity and cannot explain the full range of luminosity variations.

Accreting white dwarfs not only gain mass but also gain angular momentum. Rotation changes the mass-radius relation of white dwarfs, and at a given mass they become larger and have lower densities. Thus accreting white dwarfs can grow more massive than non-rotating white dwarfs and can reach super-Chandrasekhar masses. Yoon and Langer (2004) have calculated sequences of accreting white dwarfs with various accretion parameters. Many of their sequences resulted in rotating super-Chandrasekhar-mass white dwarfs with enough angular momentum to be dynamically stable. If these white dwarfs are Type Ia supernova progenitors, their spread in mass might be related the variance in peak luminosities. But before they can ignite, they must lose some of their angular momentum.

The same rotation that allows the white dwarf to increase its mass, can also be a cause of its demise. For high enough angular velocities, white dwarfs become secularly unstable to non-axisymmetric perturbations that emit gravitational radiation, that carries energy and angular momentum away from the star. In some cases initial perturbations are actually enhanced by the gravitational radiation and are capable of removing large amounts of angular momentum from the star. This process has been known since the 1970ies (Chandrasekhar, 1970; Friedman and Schutz, 1978) but recently it was discovered that one kind of perturbations has a much lower threshold value for the rotational velocity than other perturbations. This perturbation is called r-mode oscillation (Andersson, 1998; Friedman and Morsink, 1998).

We have investigated the angular momentum loss induced evolution of both, non-accreting super-Chandrasekhar-mass white dwarfs of various masses and initial angular momenta, and of mass and angular momentum accreting white dwarfs. Because the timescale and internal distribution of angular momentum loss due to gravitational radiation is still uncertain (Arras et al., 2003), we have tried different values for the angular momentum loss timescale. Our goal was to find out which white dwarfs are likely Type Ia supernova progenitors and how large their spread in mass, total angular momentum and angular velocity profiles is.

This paper is organized as follows: in Sect. 2, a brief theoretical introduction is given to the subject of rotating white dwarfs. We introduce the Chandrasekhar mass and the effect rotation has on maximum allowed masses, and we introduce the CFS-mechanism for angular-momentum loss and its associated timescale. The working method and experimental parameters are explained in Section 3 and the results are given in Section 4. A discussion of the results is given in Sect. 5.

2 Effects of rotation on white dwarfs

2.1 The upper mass limit of white dwarfs

The first to derive the structure of non-rotating white dwarfs, using the hydrostatic equilibrium equations, was Subrahmanyan Chandrasekhar. He used the polytrope approximation for the equation of state, that takes the pressure to be determined by the mass density alone — as is the case for completely degenerate matter — and is given by

$$P = K\rho^{\Gamma}, \tag{1}$$

with the polytrope index Γ varying between $\Gamma = 5/3$ for non-relativistic electrons and $\Gamma = 4/3$ for relativistic electrons[1]. White dwarfs above a certain mass have both an outer region where the electrons are non-relativistically degenerate and a fully relativistically degenerate core, but in the polytrope approximation one 'averages' these two regimes by taking only one value for Γ (between 5/3 and 4/3) throughout the star. As the star becomes more massive, the non-relativisticly-degenerate region becomes smaller and ultimately the most massive white dwarfs are entirely relativisticly degenerate. Chandrasekhar was the first to have shown that there is a stable solution for completely relativistic, non-rotating white dwarfs for one mass value only:

$$M = 1.457 \left(\frac{\mu_e}{2}\right)^2 \mathrm{M}_\odot, \tag{2}$$

with μ_e the mean atomic mass per electron, which has the value of 2 for carbon-oxygen white dwarfs. This critical mass defines the Chandrasekhar mass[2] $\mathrm{M_{Ch}}$ (Shapiro and Teukolsky, 1983).

Because the pressure comes from degeneracy, white dwarfs need to become smaller when they get more massive to raise the pressure enough to withstand the higher gravitational force. For low-mass white dwarfs ($\Gamma = 5/3$) the mass-radius relation is

$$R \sim M^{-\frac{1}{3}}, \tag{3}$$

and for white dwarfs approaching the Chandrasekhar limit the radius drops even faster with increasing mass.

Fig. 3 shows the carbon-ignition line, the collection of points in the central density-central temperature plane that mark the boundary between the region where carbon ignites and where it does not. These points are defined such that the energy release rate due to carbon burning equals the

[1]Sometimes the polytrope index is defined slightly different and called n. The relation between n and Γ is $\Gamma = 1 + 1/n$.

[2]Lower values are obtained when the treatment includes electrostatic pressure corrections (Ibanez-Cabanell, 1983).

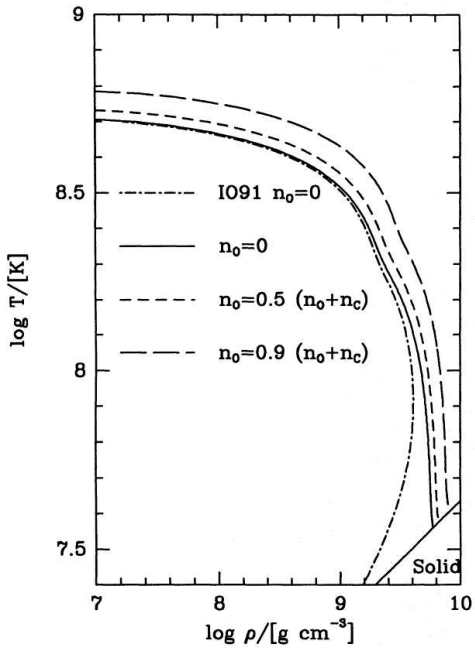

Figure 3: The central density needed for carbon ignition as function of the temperature and chemical composition of the white dwarf. $n_{\rm O}$ designates the oxygen content of the mixture and $n_{\rm C}$ the carbon content. The region marked 'solid' is the region where the white dwarf crystallizes. Figure taken from (Sahrling, 1994).

energy loss rate due to neutrino radiation at these combinations of density and temperature. The carbon fusion rate is proportional to the density and the carbon mass fraction. Thus having a lower carbon content means that the ignition density is higher. The fusion rate at temperatures lower than $\simeq 10^8\,$K is uncertain. It is not clear yet how much electron shielding at lower temperatures enhances the reaction rate hence the difference between the ignition curves from Ichimaru and Ogata (1991) (IO91 in Fig. 3) and Sahrling (1994) at the lower temperature end.

Carbon-oxygen white dwarfs with masses close to the Chandrasekhar limit have central densities of the order of $10^9\,$g cm^{-3}, high enough for the onset of carbon ignition. At $1.38\,{\rm M}_\odot$ the central density is high enough for explosive carbon ignition and since non-rotating carbon-oxygen white dwarfs are unstable above this mass as well, this critical mass is sometimes, confusingly, also referred to as Chandrasekhar mass.

The effective potential of a rotating star (gravitational potential + potential due to centrifugal force) is not spherically symmetric, but shaped like an ellipsoid, i.e. the equatorial radius of the star is larger than the polar radius. The central density of a rotating white dwarf of a given mass is lower than that of a non-rotating one with the same mass. As a result, both

gravitational collapse and carbon ignition are postponed to masses higher than the Chandrasekhar mass and $1.38\,\mathrm{M}_\odot$, respectively. The exact upper mass limit for secular and dynamical stability depends on the distribution of angular momentum inside the star. Anand (1968) has calculated that rigidly rotating white dwarfs can be dynamically stable up to $1.48 M_\odot$, and Durisen (1975) has found differentially rotating white dwarfs dynamically stable up to $4.5 M_\odot$, although these models have very short angular momentum loss timescales due to gravitational radiation.

2.2 Rotationally induced angular momentum transport

In differentially rotating stars, angular momentum can be transported between the layers. This can be described as a diffusive process with the following diffusion equation:

$$\left(\frac{\partial \omega}{\partial t}\right)_{M_r} = \frac{1}{i}\left(\frac{\partial}{\partial M_r}\right)_t \left[(4\pi r^2 \rho)^2 i \nu_{\mathrm{turb}} \left(\frac{\partial \omega}{\partial M_r}\right)_t\right] \tag{4}$$

with i the specific moment of inertia of a mass shell, ω its angular velocity and M_r its mass coordinate, defined as the mass within the radius of the mass shell. ν_{turb} is the turbulent viscosity. The turbulent viscosity is the sum of diffusion coefficients due to rotationally induced mixing processes (Endal and Sofia, 1976). Our model for white dwarfs with shellular rotation is rotating homologously and the diffusion processes we take into account are the Eddington-Sweet circulation and the dynamical and secular shear instabilities.

Rotating stars cannot be in hydrostatic and radiative thermal equilibrium at the same time. This is because surfaces of constant density, constant temperature and constant pressure do not coincide. As a result of this effect, large-scale circulations between the equator to the poles develop. The timescale of these Eddington-Sweet circulations is roughly given by

$$\tau_{\mathrm{ES}} =\simeq \tau_{\mathrm{KH}}/\chi^2 \simeq R^2/D_{\mathrm{ES}} \tag{5}$$

where τ_{KH} is the Kelvin-Helmholtz timescale and χ is the true angular velocity divided by the Keplerian value. The timescale of these circulations is very different for the core and the envelope. In the core the timescale is of the order of 10^9 yr and in the envelope it is of the order of 10^3 yr (Yoon and Langer, 2004).

For diffusion perpendicular to equi-potential surfaces the rotational gradient σ (defined as $\sigma = \partial\omega/\partial \ln r$), has to be larger than a certain critical value, given by:

$$\sigma^2_{\mathrm{DSI,crit}} \simeq 0.2 \left(\frac{g}{10^9\,\mathrm{cm\ s^{-1}}}\right)\left(\frac{\delta}{0.01}\right)\left(\frac{H_P}{8\cdot 10^7\,\mathrm{cm}}\right)^{-1}\left(\frac{\nabla_{\mathrm{ad}}}{0.4}\right) \tag{6}$$

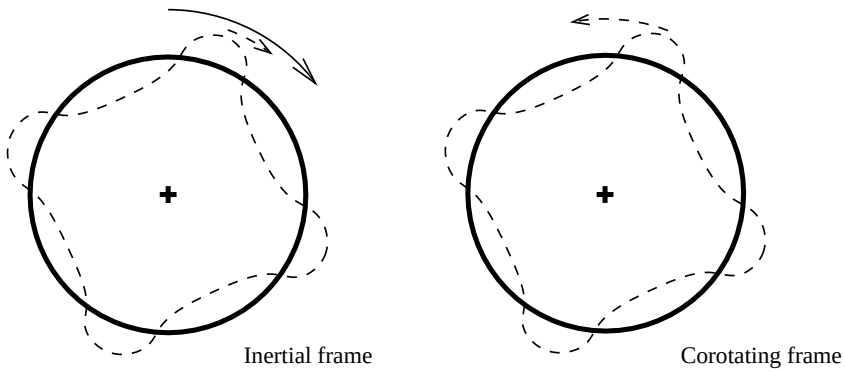

Figure 4: A necessary condition for the occurrence of the CFS-instability is that the perturbation mode moves prograde seen in an inertial frame but retrograde in an rotating frame. Seen from above, both the background (solid line) and the mode (dashed line) rotate clockwise in an inertial frame (left), but in a co-rotating frame (right) the background stands still and the mode rotates anti-clockwise.

with g the local gravity, $\delta \equiv -(\partial \ln \rho / \partial \ln T)_P$, H_P the pressure scale height and $\nabla_{\rm ad} \equiv (\partial \ln T / \partial \ln P)_s$.

By allowing for thermal diffusion, the criterion for the shear instability can be relaxed, and it no longer works on dynamical timescales but on thermal timescales. This instability is therefore called the secular shear instability. The diffusion coefficient for the secular shear instability is

$$D_{\rm SSI} = \frac{1}{3} \frac{K \sigma^2 Ri_{\rm c}}{N^2} \tag{7}$$

with K the thermal diffusivity, $Ri_{\rm c}$ the critical Richardson number and $N^2 = (g/H_P)(\nabla_{\rm ad} - \nabla)$ with $\nabla = (d \ln T / d \ln P)_s$ (Zahn, 1992).

2.3 The CFS-instability

It was discovered by Chandrasekhar (1970), and more generally proven by Friedman and Schutz (1978), that some perturbations are secularly unstable and capable of removing angular momentum from rotating stars. This occurs if the perturbations are coupled to a radiation field and if the perturbations carry negative canonical angular momentum in the co-rotating frame, but positive canonical angular momentum in an inertial frame (see Fig. 4). The necessary radiation field can in principle be a scalar, vector (electro-magnetic) or tensor (gravitational) field, but in this paper we look only at the possibility of gravitational radiation. This self-sustaining mechanism for angular momentum loss is called the CFS-instability and will be explained for one kind of perturbation in the next sub-section.

2.3.1 r-mode oscillations

Gravitational radiation occurs, among other possibilities, due to rotating mass-current quadrupole moments. These are not present in rotationally symmetric stars, but stars that rotate are prone to develop Rossby waves, that do have significant mass-current quadrupoles and it is shown by Andersson (1998) and Friedman and Morsink (1998) that so-called Rossby waves are CFS-unstable. In astrophysics Rossby waves are usually called r-mode oscillations and here we will follow this convention. r-mode oscillations and their impact on stellar evolution have been described by Lindblom et al. (1998; 2002), Levin and Ushomirsky (2001) and others.

r-mode oscillations can be decomposed into spherical harmonical modes, and we have focussed our work on the strongest one only, the $l = m = 2$-mode. The rest of the discussion is about this mode only. The r-mode oscillation is caused by the Coriolis force, is non-radial, and its velocity field is described by

$$\vec{v} = \alpha r \omega \, \mathrm{Re}\left(\vec{Y}_{22}^{\mathrm{B}}\right), \tag{8}$$

with α a dimensionless constant and $\vec{Y}_{22}^{\mathrm{B}}$ the magnetic vector spherical harmonic[3]. Hereafter we will define the average angular velocity of a star as Ω and the angular velocity of individual layers as ω. A map of the velocity field on a shell surface is given by Fig. 5. The angular velocity of the flow pattern (ς) is linked to the angular velocity of the star:

$$\varsigma_i = \frac{2}{3}\Omega \tag{9}$$

for an inertial observer or

$$\varsigma_r = -\frac{1}{3}\Omega \tag{10}$$

for an observer rotating with the star. Thus the canonical angular momentum is negative in the co-rotating frame. The angular momentum of the mode depends on the amplitude and the angular velocity. Because the gravitational radiation removes angular momentum from the mode, thus making it more negative in the co-rotating frame, either the amplitude needs to increase or the angular velocity needs to decrease (i.e. becoming more negative in the co-rotating frame), but the latter is fixed to the angular velocity of the star, thus it is the amplitude that changes. In principle the amplitude could rise until the combined angular momentum of the unperturberted background and the mode is zero, but viscosity limits the amplitude to a certain saturation value. This does not mean that the radiation reaction stops, because the gravitational radiation still takes angular momentum away. But

[3]The magnetic vector spherical harmonic is defined as $\vec{Y}_{22}^{\mathrm{B}} = \hat{r} \times r\vec{\nabla} Y_{22}/\sqrt{6}$. 'Magnetic' refers to the way the quantity behaves under parity transformation (Thorne, 1980, Eq. 2.18b).

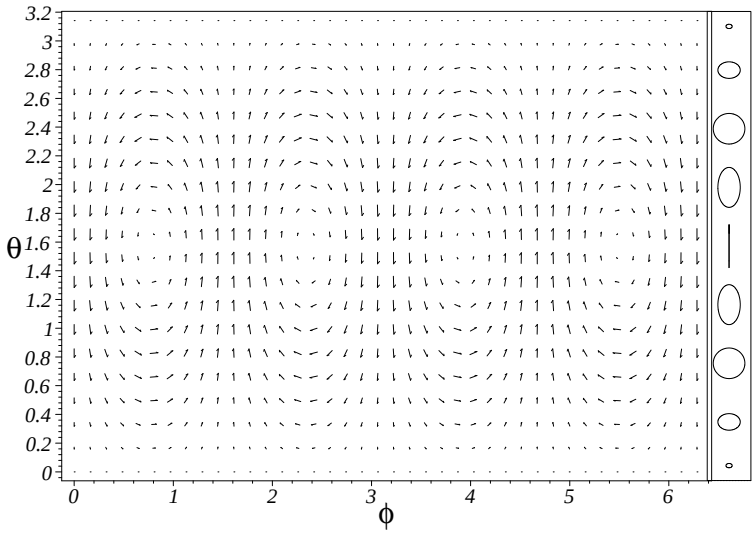

Figure 5: The velocity field of the $l = m = 2$ r-mode at an instant in time. The actual motion of individual fluid elements due to the rotation of the velocity field is pictured on the right. Figure taken from (Andersson and Kokkotas, 2001).

now the angular momentum is removed directly from the background and not from the perturbation. The time needed to reach the saturation value is very short compared to the angular-momentum-loss timescale for the r-mode, so we can take the amplitude to be at its saturation value all the time.

2.3.2 Angular momentum loss timescale

To obtain the angular momentum loss rate we calculate the associated timescale which is defined as

$$\tau_{\mathrm{GR}} \equiv \frac{J}{\dot{J}}, \tag{11}$$

with J the total angular momentum of the star and $\dot{J}$ its time derivative. In our model the star is divided into a number of mass shells labeled i, and each mass shell has its own associated loss timescale:

$$\tau_{\mathrm{GR},i} \equiv \frac{J_i}{\dot{J}_i} = \frac{j_i}{\dot{j}_i}, \tag{12}$$

with J_i the angular momentum of shell i and j_i the specific angular momentum of this shell. τ_{GR} can now be rewritten in terms of $\tau_{\mathrm{GR},i}$ as

$$\tau_{\mathrm{GR}} = \frac{J}{\dot{J}} = \frac{J}{\sum_{i=0}^{M} \dot{j}_i \mathrm{dM}_i} = \frac{J}{\sum_{i=0}^{M} \frac{j_i}{\tau_{\mathrm{GR},i}} \mathrm{dM}_i}. \tag{13}$$

For the integrated angular-momentum-loss timescale for the whole star, we use the equation given by Lindblom et al. (1998):

$$\frac{1}{\tau_{\rm GR}} = A \int_0^R \rho_r \omega^6 r^6 {\rm dr}, \tag{14}$$

with $A = (2\pi/25)(4/3)^8(G/c^7)$. Actually, Lindblom et al. (1998) assume rigid rotation and keep the angular velocity outside the integral, but the amplitude of r-mode oscillations in one shell is, to first order, not linked to the amplitude of an adjacent layer since the oscillations are not in the radial direction and have no first-order density perturbations. Thus they do not cause variations in the pressure and the gravitational potential. This is why the effect can also be described using only local quantities, and thus why we substitute ω for Ω.

Combining Eqs. (13) and (14) gives

$$\begin{aligned}
\sum_{i=0}^{M} \frac{j_i}{\tau_{{\rm GR},i}} {\rm dM}_i &= JA \int_0^R \rho_r \omega^6 r^6 {\rm dr}, \\
\sum_{i=0}^{R} \frac{j_i}{\tau_{{\rm GR},i}} 4\pi r_i^2 \rho_i {\rm dr}_i &= \int_0^R JA \rho_r \omega^6 r^6 {\rm dr}, \\
\frac{j_i}{\tau_{{\rm GR},i}} 4\pi r_i^2 \rho_i &= JA \rho r^6 \omega^6, \\
\frac{1}{\tau_{{\rm GR},i}} &= \frac{JA r_i^4 \omega_i^6}{4\pi j_i}.
\end{aligned} \tag{15}$$

We have ignored the difference between summation and integration since numerically both are the same.

The debate about the saturation amplitude of the r-mode oscillation and therefore the angular momentum loss timescale is not settled. Arras et al. (2003) and others claim that $\tau_{\rm GR}$ is much larger than given by Lindblom et al. (1998), maybe evenby 10^6. We have accounted for this uncertainty by introducing the parameter f_τ that we could change for each simulated sequence. The angular momentum loss timescale of an individual layer thus becomes:

$$\tau_{{\rm GR},i} = f_\tau \cdot \frac{4\pi j_i}{JA r_i^4 \omega_i^6} = f_\tau \frac{J_i}{J} \frac{1}{A \rho_i r_i^6 \omega_i^6 {\rm dr}_i}. \tag{16}$$

The last part can be compared with Lindblom et al.'s formula, Eq. 14. An example for a rotating white dwarf is shown in Fig. 6.

In principle, there may be other ways for rotating white dwarfs to lose angular momentum. Therefore we have also performed simulations with

$$\tau_{\rm GR}(M_r, t) = {\rm Constant}. \tag{17}$$

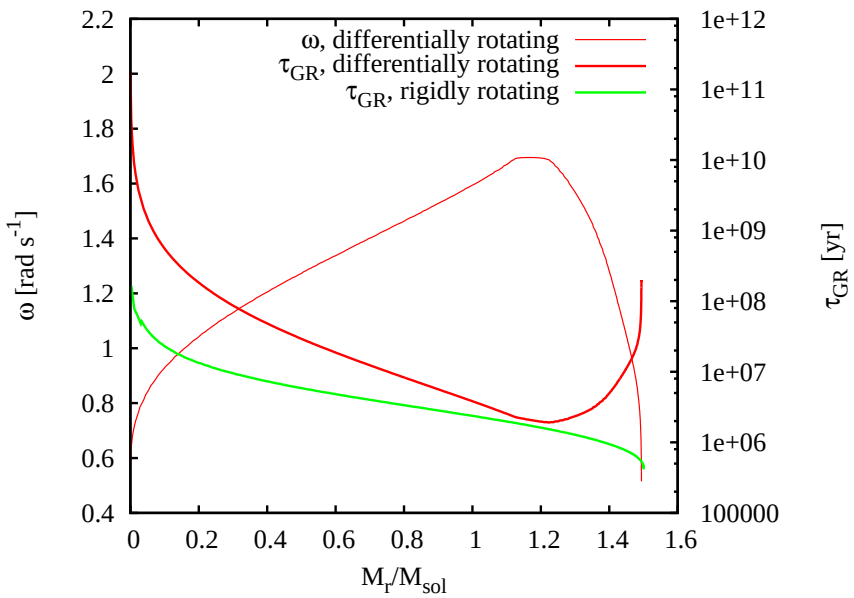

Figure 6: Initial angular velocity and angular-momentum-loss timescale distribution across a typical differentially rotating model (Sequence C2/1.5) and a nearly rigidly rotating model with $\Omega = 2.5\,\mathrm{rad\ s^{-1}}$. Both with $f_\tau = 1.0$.

3 Method

Our simulations are performed with a 1D hydrodynamic stellar evolution code (Yoon and Langer, 2004). Radiative opacities are taken from Iglesias and Rogers (1996). For the electron conductive opacity we follow Hubbard and Lampe (1969) in the non-relativistic case and Canuto (1970) in the relativistic case.

The accreted matter is assumed to have the same entropy as that of the surface of the accreting white dwarf and the accretion induced compressional heating is treated as in Neo et al. (1977). We assume that possibly present hydrogen or helium in the accreted matter is immediately converted to carbon and oxygen. This is modeled by setting the fractions of carbon and oxygen in the accreted matter to $X_C = X_O = 0.487$. In this way we neglect hydrogen and helium shell burning, but this does not influence the thermal evolution of the white dwarfs as long as rapid accretion is ensured, as shown by Yoon & Langer (2004).

Mass-transfer to non-magnetic white dwarfs in close binary systems is thought to go through a Keplerian disk. The angular momentum carried by the accreted matter is thus of about the local Keplerian value at the white dwarf equator. Yoon & Langer (2002) found that this means that the white dwarfs reach critical rotation well before they have grown to the Chandrasekhar limit. But there is a possibility, found by Paczyńsky (1991) and Popham and Naryan (1991), for angular momentum to be transported from the white dwarf to the accretion disk by viscous effect when the white dwarf rotates near break-up velocity, without preventing an uninterrupted efficient mass accretion. Based on this information we take the mass accretion rate to be constant in time. We have calculated sequences with accretion rates of $5 \cdot 10^{-7}\,\mathrm{M}_\odot/\mathrm{yr}$ and of $1 \cdot 10^{-6}\,\mathrm{M}_\odot/\mathrm{yr}$. These values are relevant for mass transfer from non-degenerate stars to white dwarfs. The angular momentum accretion rate was set to be $\dot{J}_{\mathrm{acc}} = \dot{M} \cdot j_{\mathrm{acc}}$ with j_{acc}:

$$j_{\mathrm{acc}} = \begin{cases} f \cdot j_{\mathrm{K}} & \text{if } v_{\mathrm{s}} < v_{\mathrm{K}} \\ 0 & v_{\mathrm{s}} = v_{\mathrm{K}} \end{cases} \tag{18}$$

where v_s denotes the surface velocity, v_K the Kepler velocity at the surface of the white dwarf give by $v_{\mathrm{K}} = (GM_{\mathrm{WD}}/R_{\mathrm{WD}})^{1/2}$, and j_{K} the Keplerian value for the angular momentum given by $j_{\mathrm{K}} = v_{\mathrm{K}} R_{\mathrm{WD}}$. f is a dimensionless parameter that determines which fraction of the angular momentum is actually accreted onto the white dwarf when $v_{\mathrm{s}} < v_{\mathrm{K}}$.

The angular momentum loss due to gravitational radiation, per timestep and for each mass shell, is calculated as

$$\Delta J_i = J_i(t)(1 - e^{-\Delta t/\tau_{\mathrm{GR},i}}) \tag{19}$$

with $\tau_{\mathrm{GR},i}$ being set either at a constant value ($\mathrm{d}\tau_{\mathrm{GR},i}/\mathrm{dt} = 0$ and $\tau_{\mathrm{GR},i} = \tau_{\mathrm{GR}}$), or calculated according to Eq. 16. We have assumed that the density

perturbations of the r-mode oscillation are small and have thus neglected the effect the r-mode oscillation has on the structure of the white dwarf.

Our code treats all stars as having a shellular rotation, but in reality the cores of carbon-oxygen white dwarfs may be forced to rotate cylindrically (Kippenhahn and Möllenhoff, 1974; Durisen, 1977). However, our numerical models can still represent the cylindrically rotating degenerate inner core to some degree, since most of the total angular momentum is confined at the equatorial plane in both, shellular and cylindrically rotating cases.

The dissipation of rotational energy is calculated as

$$\varepsilon_i = \frac{\mathrm{d}\mathcal{T}_i}{\mathrm{d}t} = \frac{4}{3} r\omega \frac{\mathrm{d}\omega}{\mathrm{d}t}, \tag{20}$$

with ε_i the rate per mass for the transformation from rotational energy to heat for mass shell i and $\mathcal{T}_i$ the rotational energy of this shell. During our simulations it appeared that for sequences with long angular momentum loss timescales did not behave correctly and showed bad transformations from rotational energy to heat, but most of the sequences had timescales short enough not to be bothered. If it did cause problems for a sequence this is indicated in the Results section.

The carbon-ignition line added to the $\rho_\mathrm{c}/T_\mathrm{c}$-diagrams is defined as the collection of points where, for the innermost gridpoint, the energy release rate due to carbon burning (ϵ_CC) equals the energy losses due to neutrino radiation (ϵ_ν). For ϵ_CC it was assumed that electron shielding had a significant effect on the fusion rate at lower temperatures.

We have taken the initial models for our sequences with angular momentum loss starting after the accretion phase from Yoon & Langer (2004). Sequences C2 and C10 had the same mass accretion rate ($\dot{M} = 5 \cdot 10^{-7}\,\mathrm{M}_\odot/\mathrm{yr}$) and angular momentum efficiency factor ($f = 0.30$) but different initial masses ($M_i = 0.8\,\mathrm{M}_\odot$ for C2 and $1.0\,\mathrm{M}_\odot$ for C10). The main result of the difference in initial masses is that at equal mass models from C10 have accumulated less angular momentum than models from C2. The angular velocity profile (=angular velocity as function of the mass coordinate) has a slight variance over the different models for each sequence. There is a finite time before the core of the white dwarfs has received some angular momentum from the surface and the lower mass models have not been in the accretion phase long enough to have a rotating core. The relative position of the angular velocity maximum is also not equal for all the models. But since the cause of the angular velocity profiles is the same, i.e. angular momentum deposition on the surface and diffusion through Eddinton-Sweet circulations and the two shear instabilities, and because the differences are not very large we do not consider it a parameter for our sequences and only identify them by their initial mass and angular momentum.

4 Results

4.1 Gravitational radiation after accretion, with constant timescale

The first simulations where done without using Eq. 16 for the calculation of τ_{GR}. The initial stellar model was a $1.5\,\mathrm{M}_\odot$ CO white dwarf with a rotation period of about 3 seconds. This model was constructed by letting matter and angular momentum accrete onto a $0.8\,\mathrm{M}_\odot$ white dwarf, while limiting the surface velocity to 60% of the critical velocity. This was done to mimimize the effect of bad rotational energy diffusion in this test sequences. τ_{GR} was set to a fixed value for each sequence and was equal for all individual stellar layers. The values for τ_{GR} for each sequence and a summary of the results are listed in Table 1. The final values for the gravitational energy W, the internal energy U and the rotational energy $\mathcal{T}$ are used to calculated the final value for the binding energy E_b. 'Final' means the value for the last calculated model of a sequence. In principle this might give some extra variations because not all sequences stopped at exactly the same stage of evolution, but this effect is small enough to be ignored. If the (absolute) value of the binding energy is higher than the energy that can potentially be released by carbon and oxygen burning, the star cannot prevent a collapse and can only end up as neutron star. One sequence was done with τ_{GR} according to Eq. 16 as a gauge of our local approach to gravitational radiation.

To see if models are near carbon ignition, we have plotted the central density against the central temperature and include the carbon-ignition line. This is done in Fig. 7 for the models with fixed angular-momentum-loss timescales up to 10^9 yr, and also for the gauge model with varying τ_{GR} and $f_\tau = 1.0$. For longer angular momentum loss timescales, the white dwarfs are more capable of radiating away the energy gained from contraction, with the result that the ignition line is reached at lower central temperature. There is a time lag between the moment the centre of the white dwarf crosses the carbon-ignition line (t_{cross}) and the moment the temperature starts to rise sharply because at t_{cross} the integrated energy loss by neutrino radiation is still larger than the energy release by carbon burning for the star as a whole. The temperature jump in the sequence with $\tau_{\mathrm{GR}} = 10^9$ yr is due to the spurious rotational energy dissipation, which caused nummerical problems during the sequences with long angular momentum loss timescales.

All the initial models have differential rotation, with a $\mathrm{d}\omega/\mathrm{d}r$-slope in the core that is determined by the strength of the Dynamical Shear Instability. Without angular momentum loss, this is replaced by rigid rotation after $\simeq 10^8$ yr. When the timescale for angular momentum loss is constant for each stellar shell, the timescale for the transition from differential rotation to rigid rotation stays the same. But for our gauge model, with different values for the timescale for different stellar layers, this transition timescale

Table 1: Properties of the models calculated with a constant angular momentum loss timescale. The names of the sequences are derived from the value of τ_{GR} for each sequence. The 'w/o diss.'-sequence was computed without dissipation of rotation energy. The gauge used τ_{GR} calculated using Eq. 16 with $f_\tau = 1$. The initial model (at t=0) is decribed by the mass M, the initial angular momentum J_i and the initial (mean) angular velocity Ω_i of the white dwarfs. The other values are taken at t_f, the time of the last calculated model: W_f is the gravitational energy, U_f the internal energy, $\mathcal{T}_f$ the rotational energy and $E_b = W + U + \mathcal{T}$ is the binding energy. The energy released by burning $0.5\,\mathrm{M}_\odot$ of carbon and $0.5\,\mathrm{M}_\odot$ of oxygen completely to nickel is $1.56 \cdot 10^{51}$ erg. The last two columns give the central density at the moment where the sequence crosses the carbon ignition line ($\rho_{c,ign1}$) and the moment when, integrated of the whole star, the energy release by carbon burning equals the energy losses by neutrinos ($\rho_{c,ign2}$) respectively.

No.	f_τ	M	J_i	Ω_i	t_f	W_f	U_f	$\mathcal{T}_f$	$E_{b,f}$	$\rho_{c,ign1}$	$\rho_{c,ign2}$
			10^{50}			-10^{51}	10^{51}	10^{49}	-10^{51}		
		$\mathrm{M}_\odot$	$\mathrm{g\,cm^2\,s^{-1}}$	s^{-1}	yr	erg	erg	erg	erg	$\log(\rho/\mathrm{g\,cm^{-3}})$	
$1 \cdot 10^4$ yr	-	1.5005	0.816	2.12	$3.92 \cdot 10^3$	3.23(8)	2.47(83)	9.8(45)	0.66(2)	9.23	9.28
$1 \cdot 10^6$ yr	-	1.5005	0.816	2.12	$466 \cdot 10^3$	3.65(0)	2.85(34)	10.5(4)	0.69(2)	9.38	9.45
$1 \cdot 10^8$ yr	-	1.5005	0.816	2.12	$50.3 \cdot 10^6$	4.06(2)	3.23(25)	12.0(1)	0.71(0)	9.48	
$1 \cdot 10^9$ yr	-	1.5005	0.816	2.12	$471 \cdot 10^6$	3.62(3)	2.79(12)	11.8(4)	0.71(3)	9.3	9.37
$1 \cdot 10^{10}$ yr,	-	1.5005	0.816	2.12	$896 \cdot 10^6$	2.59(5)	1.87(67)	11.7(6)	0.60(0)		
$1 \cdot 10^{10}$ yr, w/o diss.	-	1.5005	0.816	2.12	$300 \cdot 10^6$	2.45(7)	1.75(27)	12.0(7)	0.58(4)		
gauge	1.0	1.5005	0.816	2.12	$64.0 \cdot 10^3$	3.46(7)	2.68(65)	10.2(6)	0.67(8)	9.32	9.37

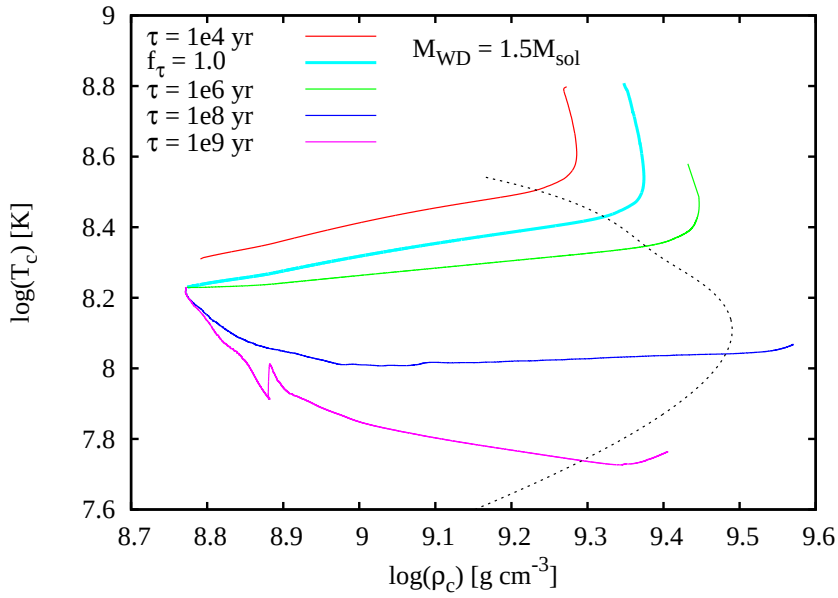

Figure 7: Evolutionary tracks in the central density and temperature plane for a $1.5\,\mathrm{M}_\odot$ white dwarf with different but constant timescales for angular momentum loss. The line labeled '$f_\tau = 1.0$' is the evolution of a gauge model with non-constant τ_{GR}. The black, dotted line is the carbon-ignition line, see section 3.

became shorter. Even though the model with $\tau_{GR} = 10^6$ yr takes about ten times as long to reach carbon ignition as the gauge model did, the former still has a much higher degree of differential rotation when they develop convective cores due to carbon ignition (Fig. 8). The rise in angular velocity over time seems to contradict the fact that the white dwarfs lose angular momentum, but it is caused by the decrease in radius. Also note that the central densities at the moment where the convective core develops are not equal due to the difference in central temperature.

For models with longer timescales than those displayed in Fig. 7 we have had some problems with spurious energy generation. This turned out to be caused by a malfunction in the routine that calculates the dissipation of rotational energy and caused temperature jumps in the ρ_c/T_c-diagrams (the $\tau_{GR} = 10^9$ yr has one as well), rendering them unusable to determine the ignition point. But as we show in the discussion, the angular-momentum-loss timescale needs to be shorter than 10^9 yr and the rotational energy diffusion worked fine for these regimes. Fig. 9 shows the very significant effect of the noisy energy dissipation on the surface temperature and Fig. 10 shows the Hertzprung-Russell diagram. Since both models are radiating like blackbodies and have equal radius, the effect is not visible in the latter figure. The bend that (most clearly) shows up in the cooling track of the sequence

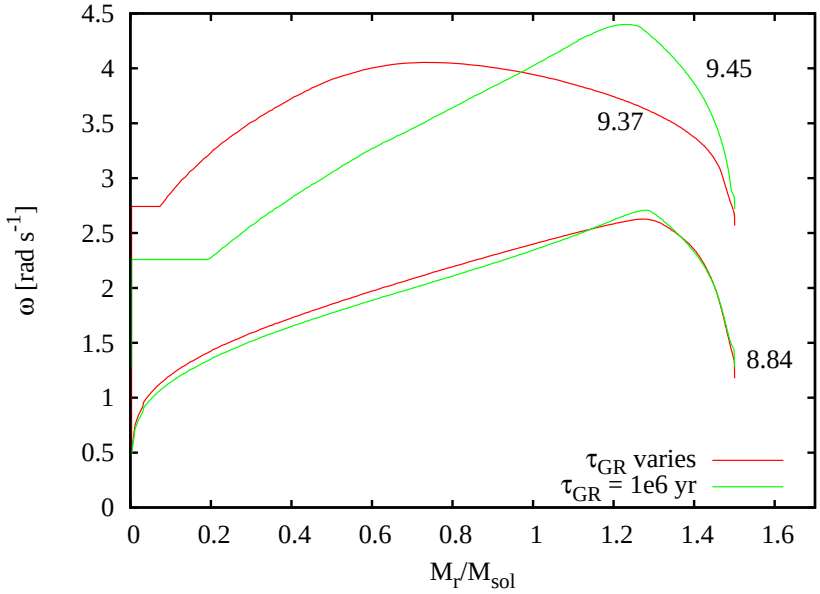

Figure 8: Time evolution of the angular velocity profile of the $1.5\,M_\odot$ model. For the case where we calculated τ_{GR} according to Eq. 16 and for a fixed value near the average of the previous case. The numbers within the graph are the logarithms of the central density. The profiles show the near-initial situation and the situation where both models have just developed convective cores.

without dissipation of rotational energy in Fig. 9, just after $t = 10^6$ yr, appears because in the beginning the outer layers are still hot from the accretion phase, and only after 10^6 yr are the stars isothermal (apart from the upper atmosphere) and show the typical long cooling timescale of white dwarfs.

4.2 Gravitational radiation after the accretion phase

Of course we wanted to see the effect of gravitational radiation in more cases than the $1.5\,M_\odot$ model. Therefore we have applied Eq. 16 to models with different masses and angular momenta. These were obtained by taking models with different masses from sequences C2 and C10 from Yoon and Langer (2004). An overview of the different models, which gives their mass and initial angular momentum, is given in Table 2, together with the final values for the gravitational, internal and rotational energy and the ignition densities according to two definitions. A natural division is made in the presentation of our results between sub-Chandrasekhar-mass models that do not ignite carbon and the super-Chandrasekhar-mass models. For our sequences the division lies somewhere near $1.37\,M_\odot$.

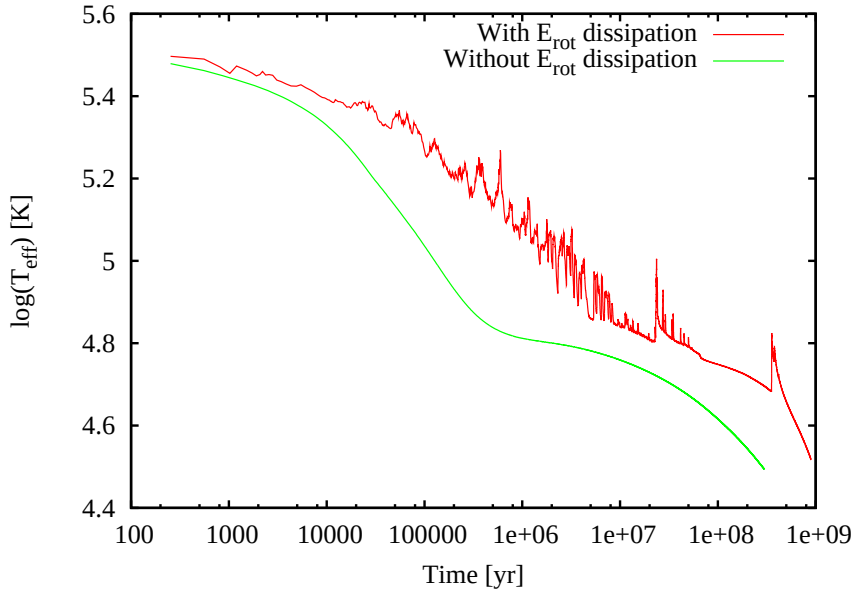

Figure 9: Effective surface temperature as a function of time for the sequence with a fixed timescale of $\tau_{GW} = 1 \cdot 10^{10}$ yr, with and without dissipation of rotation energy.

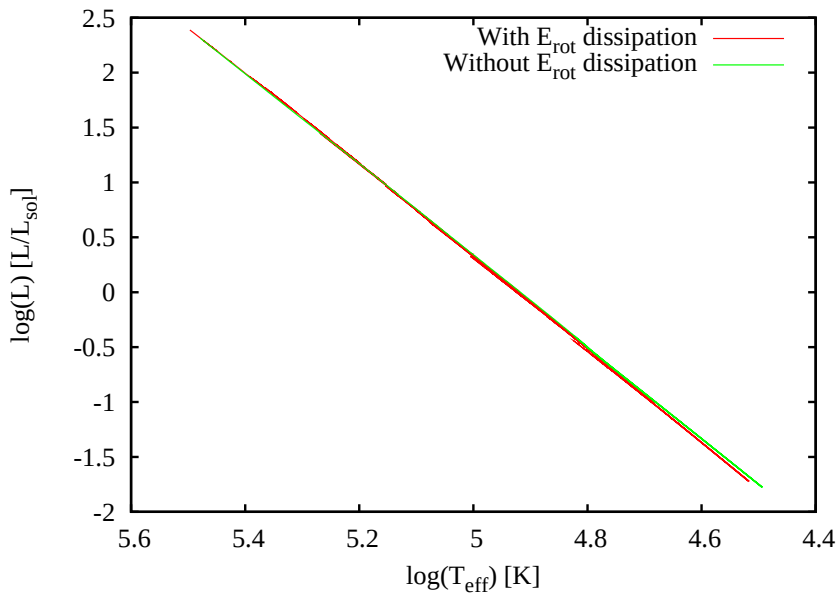

Figure 10: Hertzprung-Russell diagram for the same models as Fig. 9.

Table 2: The sequences with gravitational radiation *after* the mass accretion phase. The names for the sequences (C2/1.2 etc.) are taken from (Yoon and Langer, 2004), with the suffix giving an indication for the mass of the model. The meaning of the other columns is identical to table 1.

No.	f_τ	M	J_i	Ω_i	t_f	W_f	U_f	$\mathcal{T}_f$	$E_{b,f}$	$\rho_{c,ign1}$	$\rho_{c,ign2}$
			10^{50}			-10^{51}	10^{51}	10^{49}	-10^{51}		
		$M_\odot$	$\mathrm{g\,cm^2\,s^{-1}}$	s^{-1}	yr	erg	erg	erg	erg	$\log(\rho/\mathrm{g\,cm^{-3}})$	
C2/1.2	1.0	1.1903	0.825	0.63	$14.8 \cdot 10^9$	1.011	0.701	0.145	0.308	-	-
C2/1.3	1.0	1.2911	1.036	0.86	$16.9 \cdot 10^9$	1.706	1.289	0.127	0.416	-	-
C2/1.37	1.0	1.3672	1.193	1.04	$127 \cdot 10^6$	3.002	2.465	0.531	0.484	9.3	9.33
C2/1.4	1.0	1.3925	1.245	1.11	$13.0 \cdot 10^6$	3.677	3.090	1.225	0.575	9.49	9.59
C2/1.42	1.0	1.4179	1.297	1.17	$2.14 \cdot 10^6$	3.428	2.792	3.690	0.600	9.37	9.44
C2/1.44	1.0	1.4432	1.349	1.24	$1.05 \cdot 10^6$	3.428	2.746	5.729	0.625	9.34	9.41
C2/1.47	1.0	1.4686	1.401	1.32	$623 \cdot 10^3$	3.490	2.757	8.082	0.653	9.32	9.39
C2/1.5	1.0	1.4939	1.452	1.40	$405 \cdot 10^3$	3.499	2.724	9.830	0.677	9.30	9.37
C2/1.6	1.0	1.5952	1.657	1.76	$96.3 \cdot 10^3$	3.597	2.640	18.26	0.775	9.26	$\sim$ 9.34
C2/1.7	1.0	1.6964	1.859	2.26	$26.3 \cdot 10^3$	3.726	2.592	27.19	0.862	$\sim$ 9.24	
C10/1.2	1.0	1.1982	0.371	0.46	$15.1 \cdot 10^9$	1.048	0.731	0.141	0.315	-	-
C10/1.3	1.0	1.2996	0.556	0.86	$14.4 \cdot 10^9$	1.799	1.370	0.165	0.428	-	-
C10/1.4	1.0	1.4007	0.733	1.39	$4.47 \cdot 10^6$	3.770	3.158	1.933	0.592	9.47	9.58
C10/1.5	1.0	1.5018	0.906	2.05	$85.8 \cdot 10^3$	3.436	2.655	10.50	0.676	9.30	9.34
C10/1.6	1.0	1.6003	1.069	2.95	$9.92 \cdot 10^3$	3.445	2.501	18.32	0.761	9.24	
C10/1.7	1.0	1.7013	1.233	4.26	$1.25 \cdot 10^3$	4.015	2.836	30.94	0.869	9.31	

4.2.1 Sub-Chandrasekhar-mass white dwarfs

Fig. 11 shows that the models with the lowest masses (1.2 and $1.3\,\mathrm{M}_\odot$) are not massive enough to reach the densities and temperatures needed for carbon ignition after their spin down. After a certain period of cooling and slowing down, the central densities reach their final values. Since the release rate of rotational and gravitational energy is slower than the radiation rate of the stars, they have no heating-up period. The central and surface temperatures of the stars decline monotonically (apart from some fluctuation in the surface temperature). The bend in the cooling track (Fig. 13) is again an effect of the outer layer initially being much hotter than the interior. If the surface temperature and luminosity are put together in a Hertzprung-Russel diagram (Fig. 12) one sees that white dwarfs of the same mass again follow the same track. The perturbation seen in three of the sequences is caused by spurious rotational energy diffusion.

Fig. 14 shows that these seqences end in stable white dwarfs. After 1 Gyr the radii do not decrease anymore and the central densities stay below $10^9\,\mathrm{g\ cm^{-3}}$. The angular momentum keeps decreasing, but at a continously increasing timescale. The central temperature of some sequences (most visibly C2/1.3) show signs of the spurious rotational energy diffusion.

We find that the white dwarfs are still rotating rapidly after 14 Gyr, with periods ranging from 21 to 27 s, even though our assumption for the strength of the gravitational radiation might be optimistic. The rise in surface velocity in the first 10^5 yr is the result of a combination of the following effects. During the accretion phase the layers just below the surface rotate faster than the surface itself and angular momentum diffusion after accretion raises the surface velocity. The second effect is the cooling after the accretion phase as described in the previous paragraph, which makes the surface layers contract.

4.2.2 Super-Chandrasekhar-mass white dwarfs

Fig. 15 shows the evolution of some key quantities for models of various masses. The T_c/t-plot shows the division between white dwarfs that contract fast enough to heat their core before carbon ignition and white dwarfs that contract slow enough to radiate the released gravitational energy away without heating. The top graph shows that more massive white dwarfs have indeed smaller radii than less massive ones, even if they posses more angular momentum. The central density of sequence C2/1.37 shows signs that it has nearly reached the value equal to that of a non-rotating $1.37\,\mathrm{M}_\odot$ white dwarf. This is important for its further evolution, but that will be discused later on in this section.

For sequences with masses below $1.5\,\mathrm{M}_\odot$ the angular-momentum-loss rate ($\mathrm{d}J/\mathrm{d}t$) is a monotonically decreasing function of time, but not for

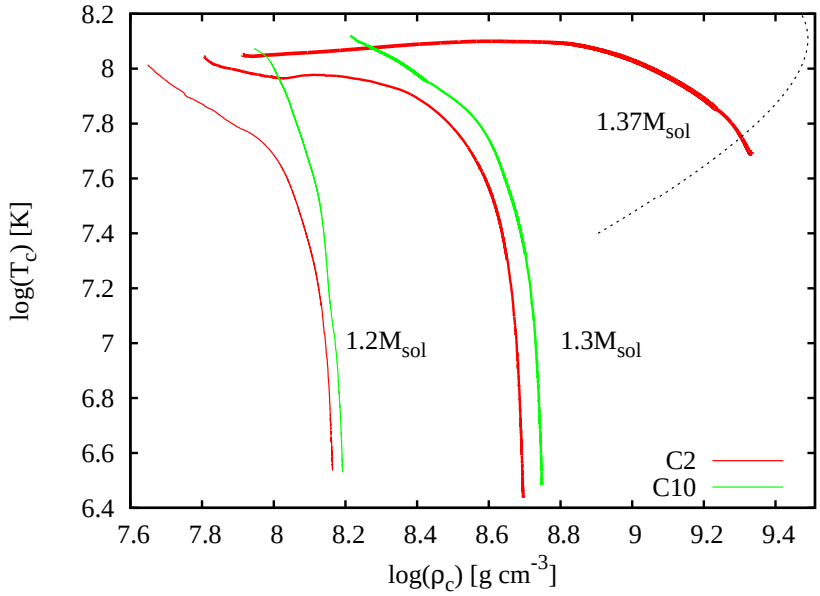

Figure 11: Evolutionary tracks in the central density and temperature plane for sub-Chandrasekhar-mass white dwarfs, the $1.37, \mathrm{M}_{\odot}$ model has been included for comparison. The sub-Chandrasekhar mass models have evolved for at least 14 Gyr. Sequences of equal denoted mass do not converge because there is a slight variation in the actual masses, see table 2 for the exact figures.

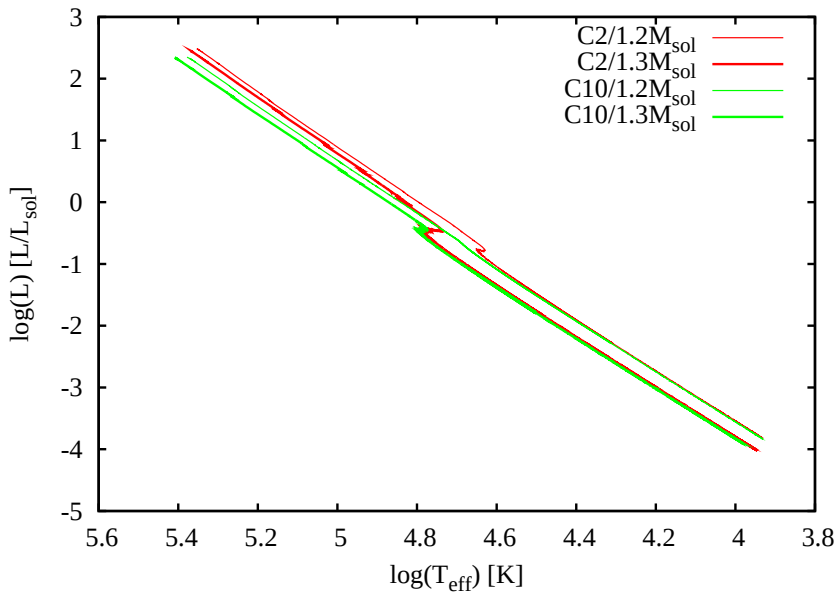

Figure 12: Hertzprung-Russell diagram of sub-Chandrasekhar-mass white dwarfs with different masses and initial angular momenta.

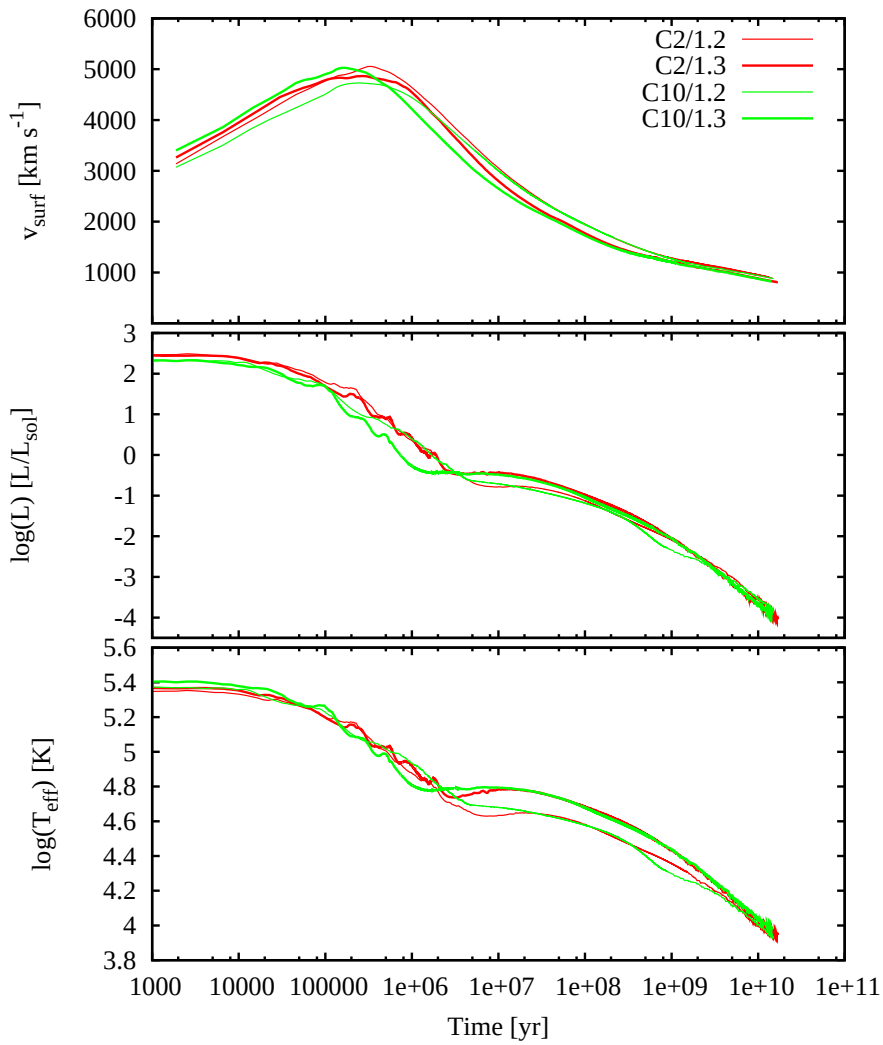

Figure 13: $T_{\rm eff}$, L and $v_{\rm surf}$ as functions of time for sub-Chandrasekhar-mass white dwarfs with different masses and initial angular momenta.

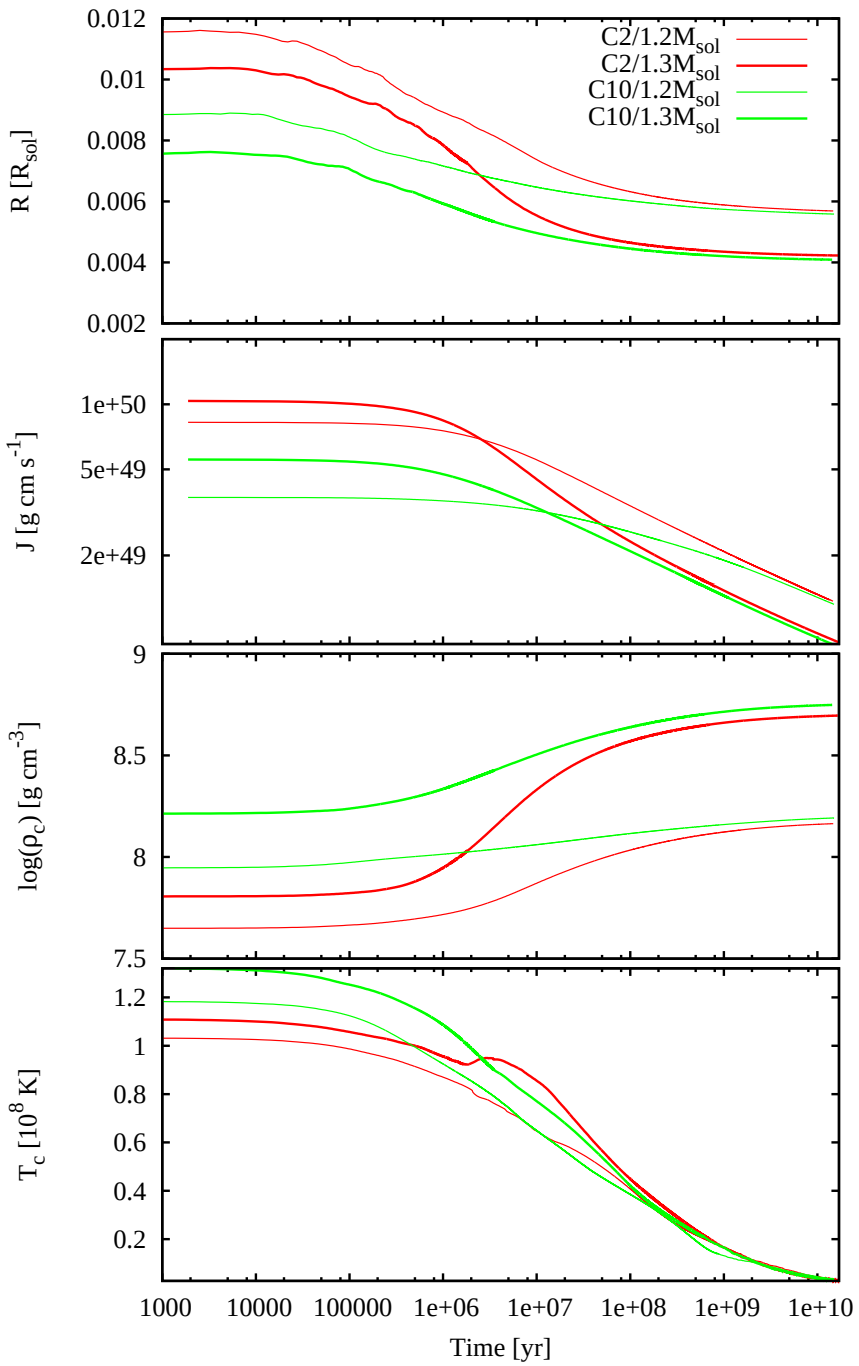

Figure 14: Radius, angular momentum, central density and central temperature as functions of time for sub-Chandrasekhar-mass white dwarfs.

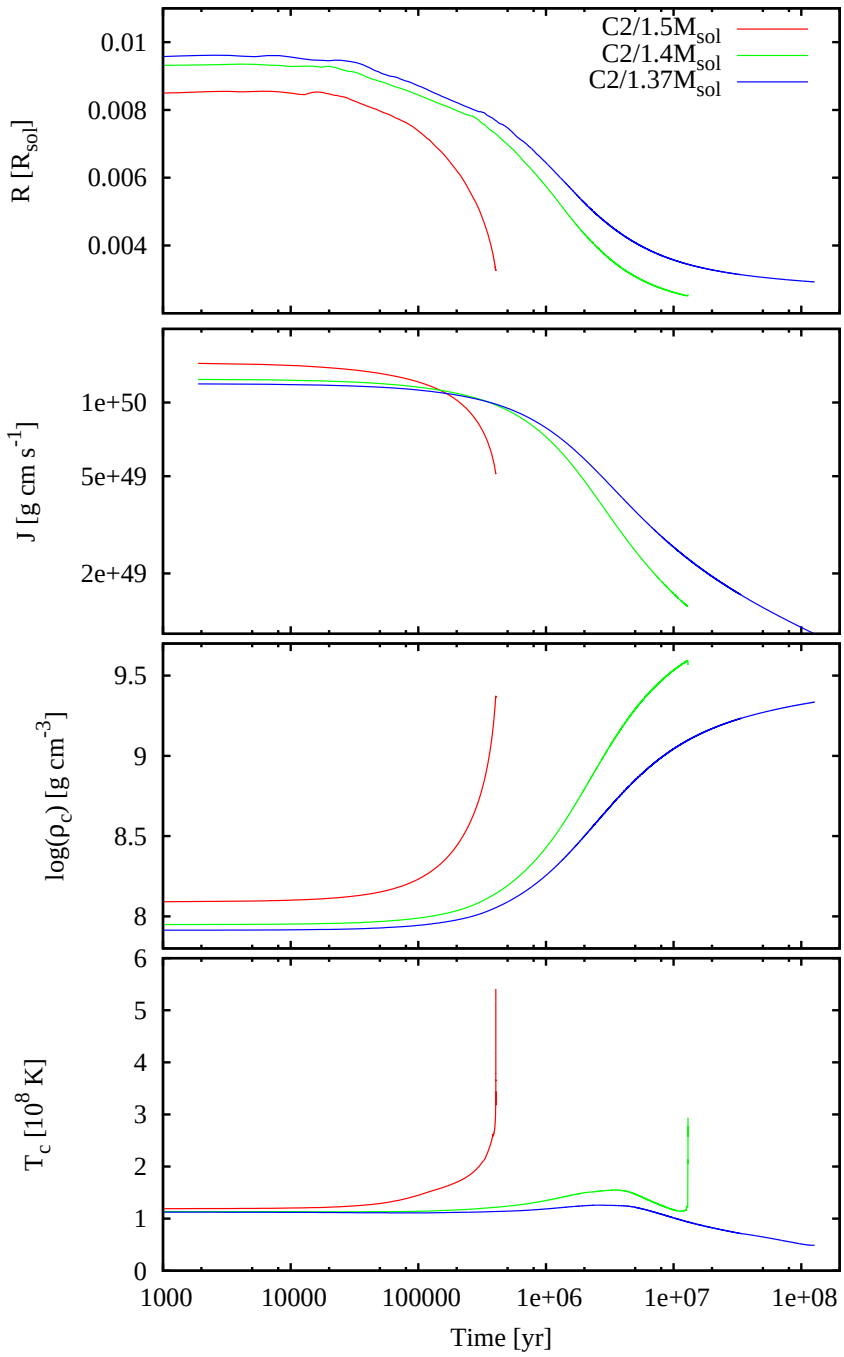

Figure 15: Radius, total angular momentum, central density and central temperature as functions of time for sequence C2/1.37, C2/1.4 and C2/1.5.

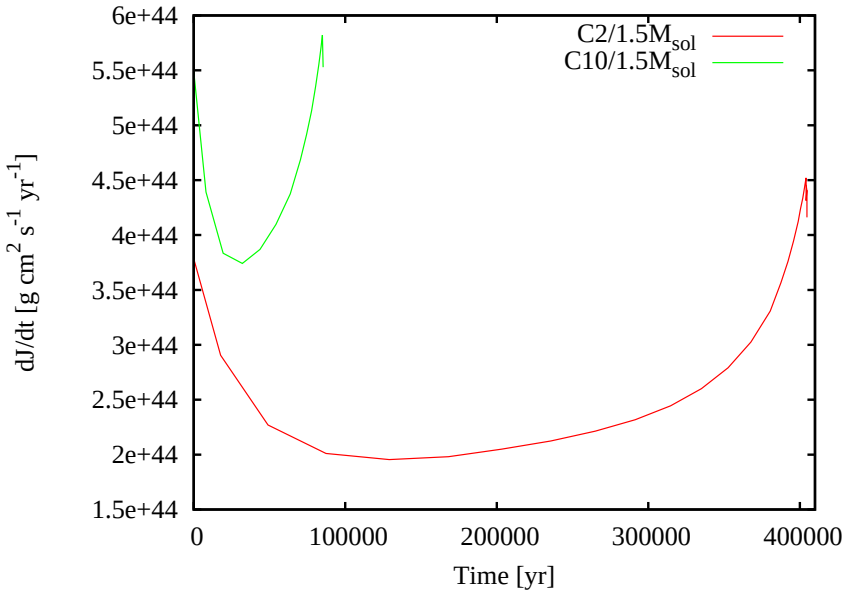

Figure 16: Angular momentum loss rate as function of time for sequences C2/1.5 and C10/1.5.

sequences with $M \geq 1.5\,\mathrm{M}_\odot$ (Fig. 16). Initially $\dot{J}$ falls of with decreasing angular momentum, but ultimately it rises again because the radius keeps decreasing and ω increases. The small drop at the very end is caused by ignition-induced expansion. C10/1.5 has a higher angular momentum loss rate, even though it has lower initial angular momentum, because its initial rotation period is shorter. The initial angular velocity profile of C2/1.5 is shown in Fig. 6, that of C10/1.5 has a similar shape, but C10/1.5 has a higher maximum angular velocity. Profiles at later epochs are shown in Fig. 17. Because gravitational radiation removes most of the angular momentum from the outer layers, and it takes longer for C2/1.5 to reach carbon ignition, its angular momentum at the moment of ignition is concentrated much more to the core than that of C10/1.5.

Fig. 18 shows the ρ_c/T_c-evolution tracks of the super-Chandrasekhar-mass sequences for the models for which we could compare the influence of the initial angular momentum. The sequences of C10 start at higher densities than the sequences of C2 because their initial angular momentum is lower. The $1.7\,M_\odot$ models are very short lived. They reach the carbon ignition line less than $3{\cdot}10^4$ yr after the end of accretion and the beginning of gravitational radiation, while it takes $127{\cdot}10^6$ yr for sequence C2/1.37 . This is important because the carbon-ignition curve is temperature dependent. If it takes longer for a model to reach it, it would do so at lower temperature and thus at a higher central density.

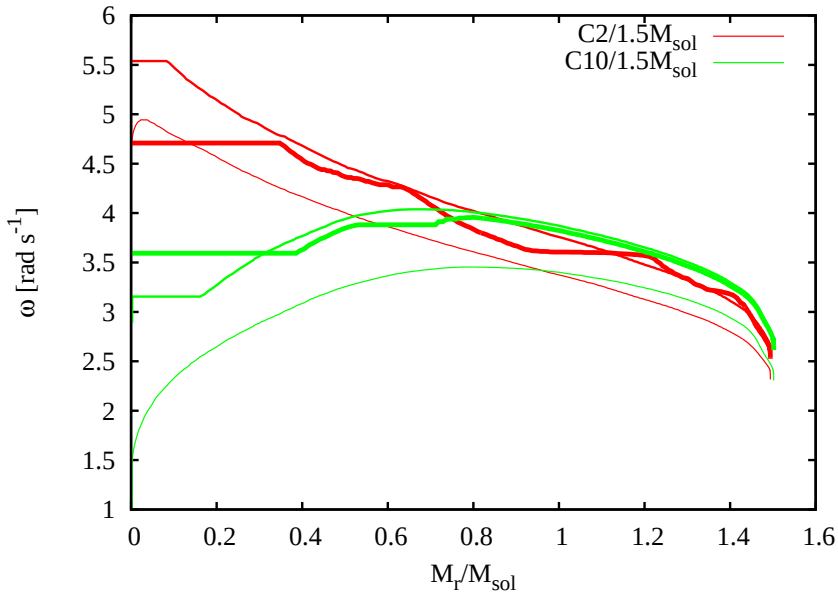

Figure 17: Evolution of the angular velocity profile of two $1.5\,\mathrm{M}_\odot$ models with different initial angular momentum (C2/1.5 and C10/1.5). The profiles are for $\log(T_\mathrm{c}) = 8.42$, 8.50 and 8.70 (thin, medium and thick lines respectively).

Figure 19 shows the ρ_c/T_c-evolution tracks of the super-Chandrasekhar-mass sequences with masses ranging from 1.37 to $1.7\,M_\odot$. The further evolution of the $1.37\,M_\odot$ model after crossing the ignition line is unclear. If the central temperature rises due to carbon ignition, it will cross the ignition line again. It is possible that white dwarfs reaching the ignition line below the bend will follow it, quiescently burning carbon, and have runaway ignition when they reach the turning point of the ignition line. If this is the case, then there is a range of masses for which white dwarfs will only have runaway carbon burning if the contraction is fast enough to heat their interior and reach the ignition line above the bend. These are the masses for which non-rotating models have a central density below $\simeq 3.1 \cdot 10^9\,\mathrm{g\ cm^{-3}}$, the density value of the turning point. Because if white dwarfs with these masses reach the ignition line below the bend, they cannot follow it up to the point where they can have runaway carbon burning. Sequence C2/1.37 is likely to be a member of the latter group since its central density increases only very slowly near the end of the computations, like it allready has reached its maximum value.

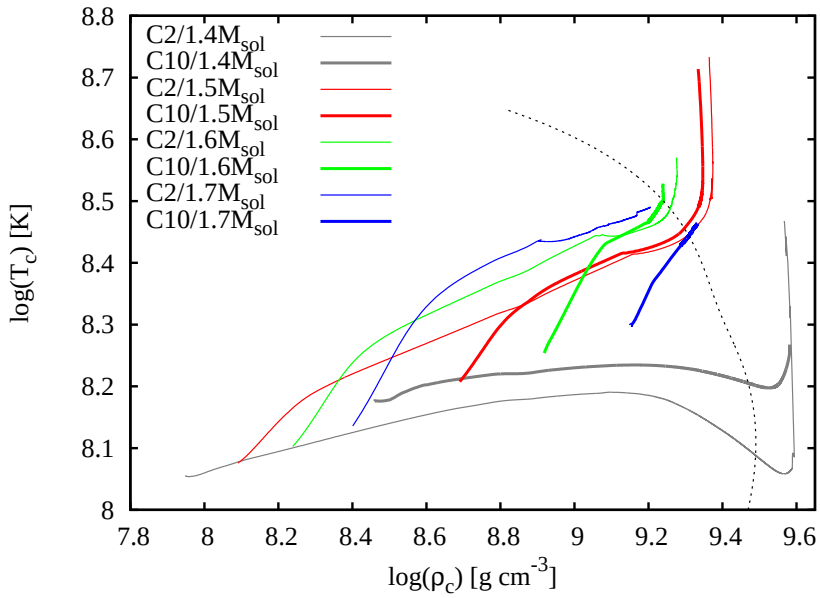

Figure 18: Evolutionary tracks in the central density and temperature plane for super-Chandrasekhar-mass white dwarfs of which we have calculated two sequences per mass, differing in intitial angular momentum.

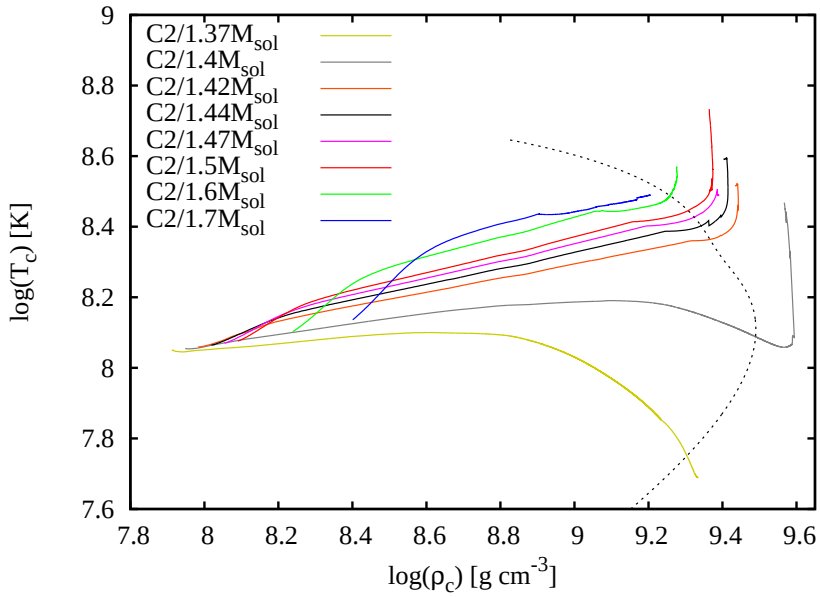

Figure 19: Evolutionary tracks in the central density and temperature plane for super-Chandrasekhar-mass white dwarfs of various masses.

4.3 Gravitational radiation during the accretion phase

If the white dwarf is quiescent enough during the accretion phase (i.e. is not turbulent or convective), r-mode oscillations might be present at this stage as well. Therefore we have repeated some of the simulations of accreting white dwarfs done by Yoon and Langer (2004), including angular momentum loss due to gravitational radiation waves. We wanted to see the influence of the following parameters: f, $\dot{M}$, M_i and f_τ. The sequence numbers are taken from this article, with lower-case letters added to distinguish between different values for f_τ. The list of sequences with the parameter settings, initial properties and the values of some quantities at ignition-time is given in Table 3.

The strength of the gravitational radiation has a large impact on the white dwarf evolution. With $f\tau$ set to 1.0, the white dwarf grows to a mass of $1.55\,\mathrm{M}_\odot$, with $f\tau = 10$ this becomes $1.72\,\mathrm{M}_\odot$ and without gravitational radiation the mass could grow beyond $1.86\,\mathrm{M}_\odot$. Langer et al. (2000) have shown that mass-transfer periods can be long enough to reach these masses. The presence of gravitational radiation influences the angular velocity profile only mildly. With less strong gravitational radiation the maximum angular velocity is located a bit nearer to the surface. Fig. 20 shows that the sequences with less or no angular momentum loss due to gravitational radiation evolved slower in the ρ_c/T_c-plane.

Fig. 21 compares the evolution of sequences C2a, C4a, C10a and A2a. The radius of the sequence with a larger initial mass (C10a) starts smaller and stays smaller. The radius of the sequence with the highest accretion rate (C4a) is larger because the outer layers are more bloated by the higher accretion-induced heating than those of C2a and A2a. The radius of A2a rises at the moment of carbon ignition; the calculations of the other sequences stops before this happens.

The origin of the small temperature jumps that all sequences experience between reaching 1.2 and $1.4\,\mathrm{M}_\odot$ is unknown.

From the angular momentum as function of time (Fig. 21) we can derive that altough C2a accepted only up to 30% of the Keplerian value of the angular momentum, and A2a up to 100%, this has a small effect on the total amount of angular momentum. This is because the surface velocity of sequence A2a reached the critical velocity much faster than C2a did. Fig. 22 shows that A2a did not accept a large part of the angular momentum it could potentially receive due to the condition in Eq. 18.

The angular momentum accretion rate of C2a can be taken to be nearly equal to $f j_K \dot{M}$, and this assumption is made in Fig. 23. The angular momentum accretion rate is fairly constant in time. The angular momentum loss rate by gravitational radiation is initially very low because the spin velocity of the star is still low. The increase is caused by the increase in angular momentum due to accretion and because τ_{GR} becomes smaller as

Table 3: Properties of the models including angular momentum loss *during* the accretion phase. The $0.8\,\mathrm{M}_\odot$ sequences started with an initial angular momentum of $1.831 \cdot 10^{47}\,\mathrm{g\,cm^2\,s^{-1}}$ and the $1.0\,\mathrm{M}_\odot$ sequence with an angular momentum of $1.704 \cdot 10^{47}\,\mathrm{g\,cm^2\,s^{-1}}$. $\dot{M}$ is the mass accretion rate, f the angular momentum accretion efficiency and M_i the initial mass. The meaning of the other columns is identical to Table 1. The value between brackets is not given at the time of core ignition but at carbon shell ignition.

No.	$\dot{M}$	f	f_τ	M_i	t_f	M_f	W_f	U_f	$\mathcal{T}_f$	$E_{b,f}$	$\rho_{c,ign1}$	$\rho_{c,ign2}$
	10^6				10^6		-10^{51}	10^{51}	10^{49}	-10^{51}		
	$\mathrm{M}_\odot/\mathrm{yr}$			$\mathrm{M}_\odot$	yr	$\mathrm{M}_\odot$	erg	erg	erg	erg	$\log(\rho/\mathrm{g\,cm^{-3}})$	
C2a	0.5	0.3	1.0	0.80	1.50	1.5509	3.6193	2.7472	14.556	0.726	9.29	9.35
C2b	0.5	0.3	10	0.80	1.84	1.7209	3.5227	2.3912	27.793	0.854		
C2d	0.5	0.3	∞	0.80	2.13	1.8626	2.8464	1.6833	54.812	0.615		
C4a	1.0	0.3	1.0	0.80	0.80	1.5992	3.0252	2.1341	16.994	0.721		(9.06)
C10a	0.5	0.3	1.0	1.00	0.98	1.4886	3.4196	2.6743	9.4498	0.651	9.31	9.36
A2a	0.5	1.0	1.0	0.80	1.51	1.5565	3.6376	2.7505	15.537	0.732	9.28	~ 9.4

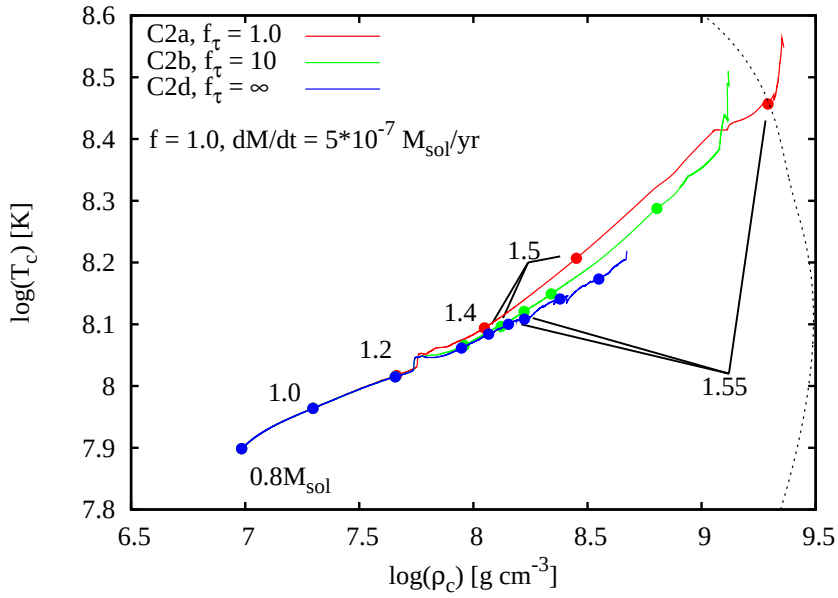

Figure 20: Evolutionary tracks in the central density and temperature plane for two sequences with different multiplier factors for the angular-momentum-loss time scales. The unlabeled dots denote 1.6 and 1.7 (green line) and 1.6, 1.7 and 1.8 (blue line).

the angular velocity increases and the radius decreases. After the white dwarf has reached a mass of $\simeq 1.4\,M_\odot$, the star looses more angular momentum by gravitational radiation than it receives by accretion and the angular momentum no longer increases, but starts to decrease.

Fig. 24 shows the rotation profiles of sequences C2a and A2a. Since both sequences have effectively the same angular momentum accretion rate, both profiles are nearly equal. During the last stages of evolution the angular velocity rises very fast because the radius shrinks, but until the convection in the core due to carbon burning makes the core rotate rigidly, the profile does not change. C4a's angular momentum profile (not visible in graph) develops in a similar way. The velocity profile of C10a (not visible in graph) starts with the fastest rotation located more to the surface, but by the time the core becomes convective, the distribution of angular velocity has become similar to that of the other sequences.

The angular velocity profile is reflected also in the strength of rotational mixing. Just like Fig. 24, Fig. 25 shows that angular momentum reaches the core when the white dwarf of sequence C2a is about $1.25\,M_\odot$. After this time the degree of differential rotation decreases and the rotational mixing disappears again.

The sequences with different angular momentum accretion efficiency

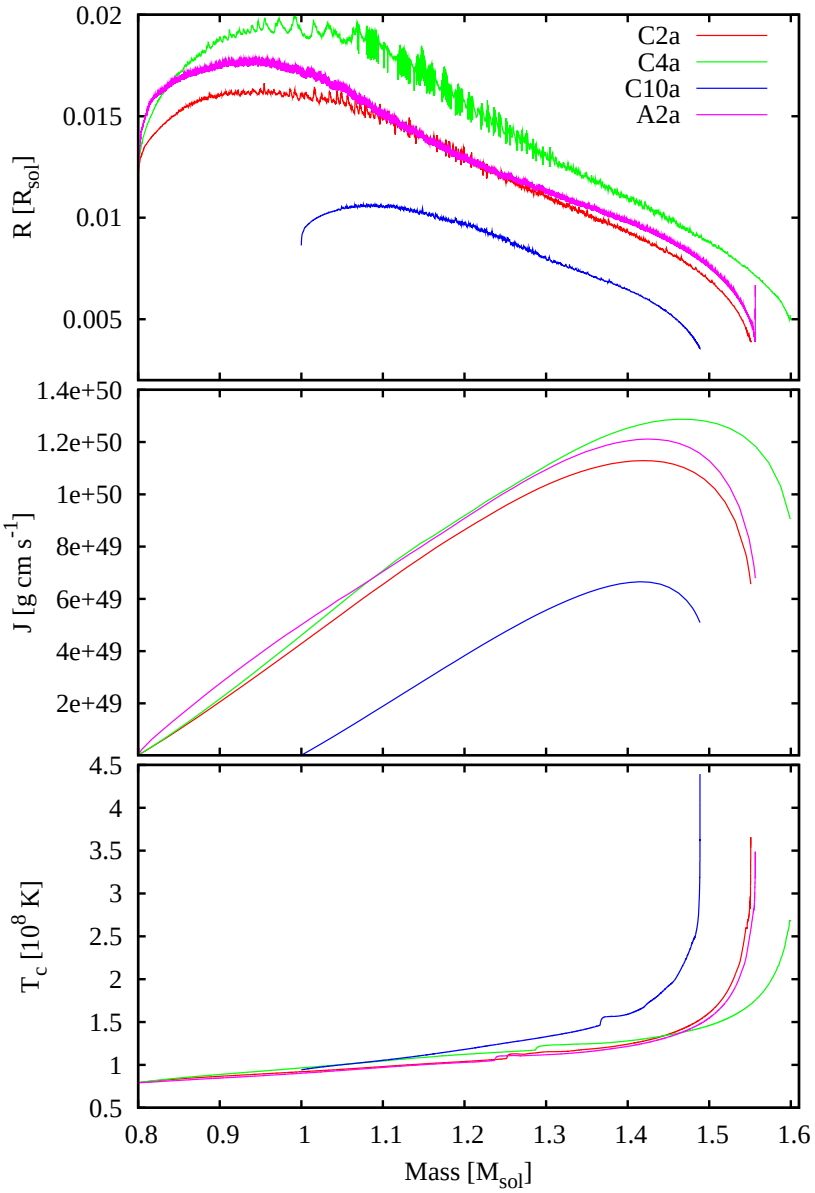

Figure 21: Radius, total angular momentum and central temperature as functions of mass (which serves as a linear measure of time) for sequence C2a, C4a, C10a and A2a.

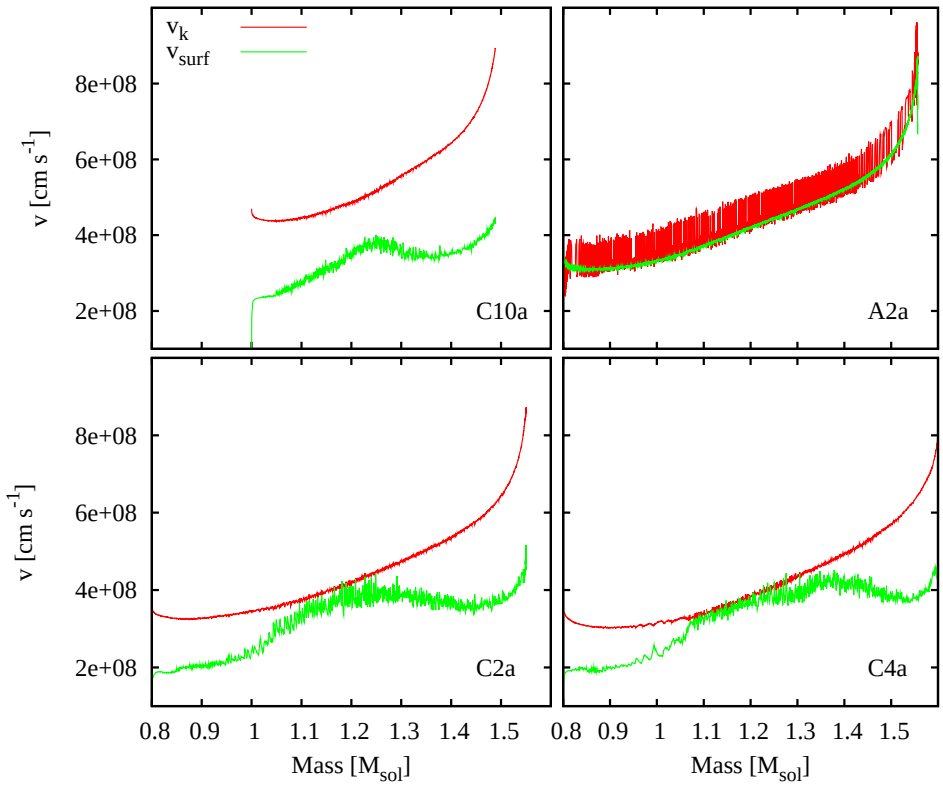

Figure 22: Comparison between the surface velocity and the equatorial Kepler velocity just above the surface as functions of mass for sequences C2a, C4a, C10a and A2a.

(C2a and A2a) follow almost the same ρ_c/T_c-track (Fig. 27) and the difference in the ignition mass and density is only a few percent. The sequence with a higher initial mass (C10a) ignites at a somewhat lower mass (Fig. 28).

A higher accretion rate (C4a) leads in our case to shell carbon-ignition. The energy deposition rate in the outer layers is proportional to the accretion rate and in this case the extra heat cannot be radiated away sufficiently enough. The shell carbon-burning starts $3.5 \cdot 10^5$ yr after the onset of accretion, but it takes another $5 \cdot 10^5$ yr before it dominates over the neutrino losses. The carbon burning begins at a mass coordinate of $1.07\,\mathrm{M}_\odot$ while the white dwarf has a mass of $1.15\,\mathrm{M}_\odot$. Fig. 26 shows that the burning initially stays confined to a small layer, this is because of the high neutrino losses. The ignition cannot be seen on this scale but was well resolved in the calculations. The maximum energy release rate by carbon burning at the end of the computations was $3 \cdot 10^9\,\mathrm{L}_\odot$. Fig. 29 shows that the central density and temperature where not sufficiently high for carbon ignition yet. Thus the $\rho_{c,ign2}$ value for this sequence is for the moment when the energy

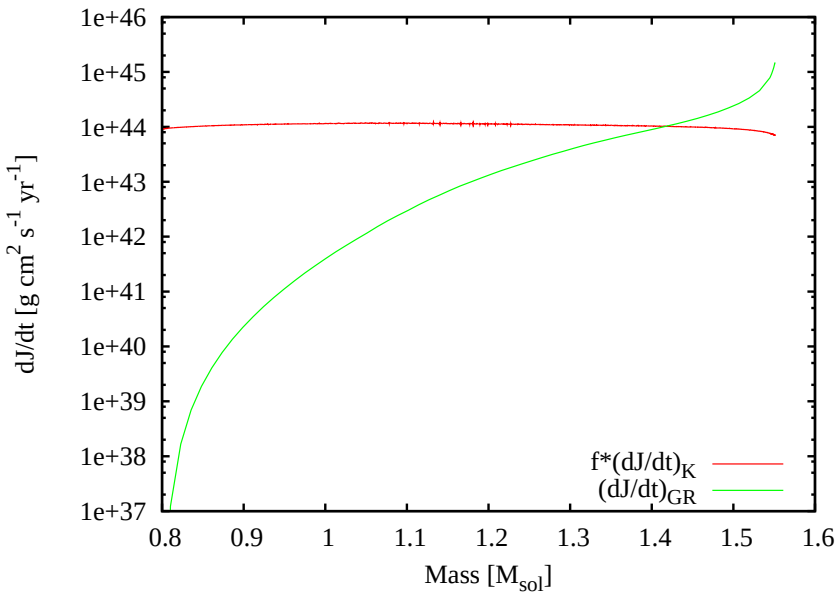

Figure 23: Angular-momentum gain due to accretion and loss due to gravitational radiation as functions of mass for sequence C2a.

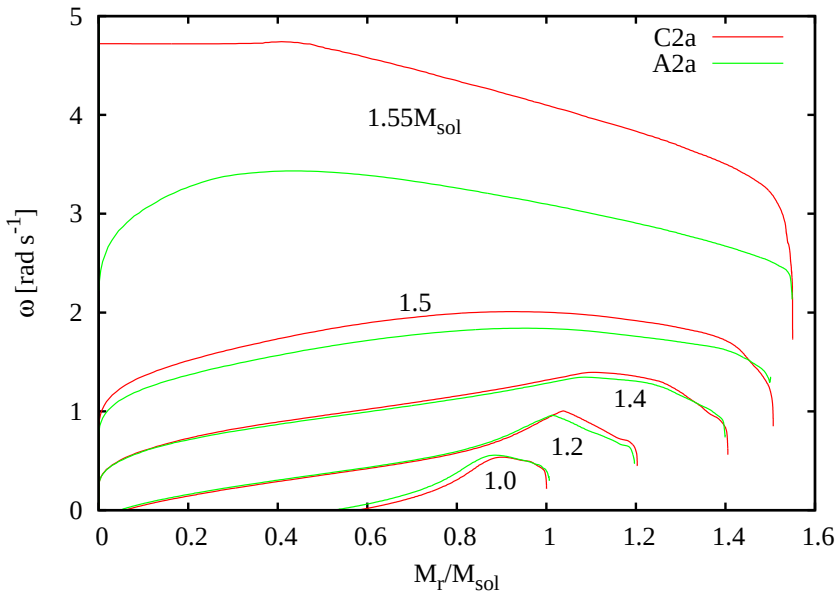

Figure 24: Evolution of the angular velocity profiles of two sequences with different angular momentum gain factors f. The numbers within the graph denote the white dwarf mass in solar masses.

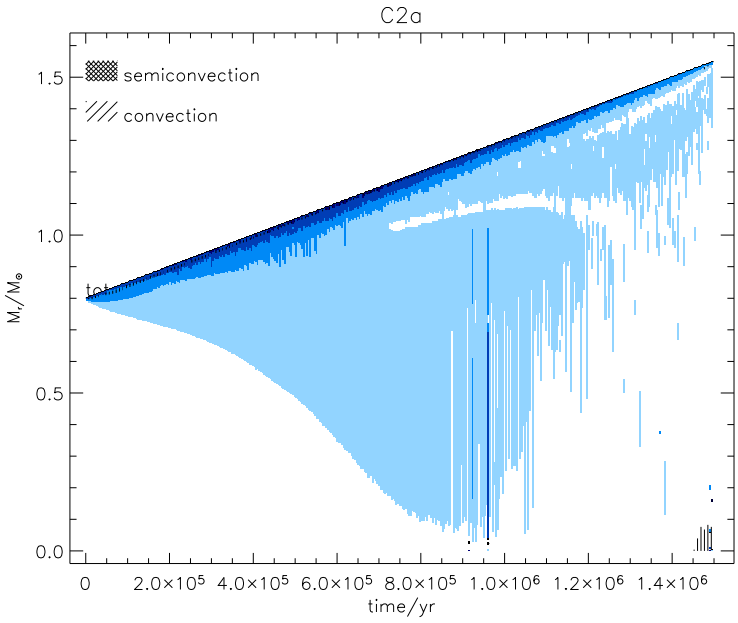

Figure 25: Plot showing the convective (diagonal hatching) and burning (vertical hatching) regions and the strength of rotational mixing (darker shades of blue meaning stronger mixing) for sequence C2a. The convective core is not visible on this scale.

release by shell carbon-burning equals the neutrino losses, not when central carbon-burning equals neutrino losses.

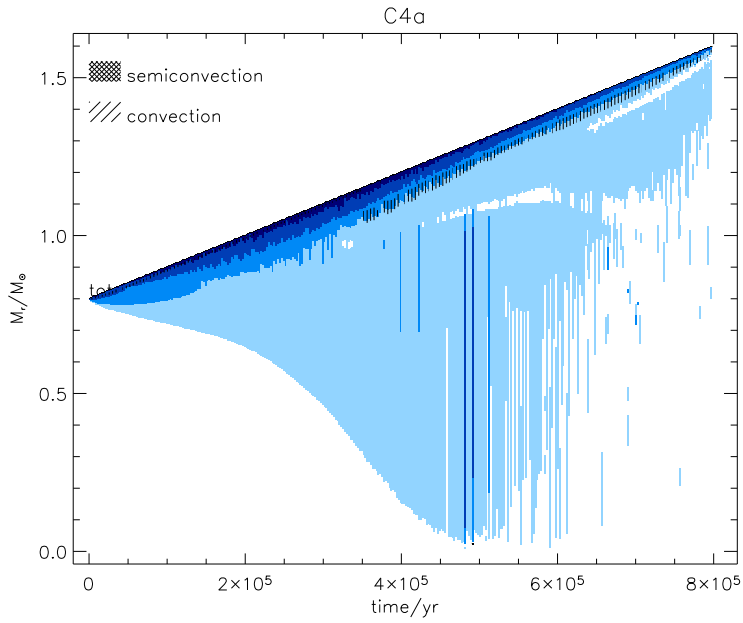

Figure 26: Plot showing the convective (diagonal hatching) and burning (vertical hatching) regions and the strength of rotational mixing (darker shades of blue meaning stronger mixing) for sequence C4a.

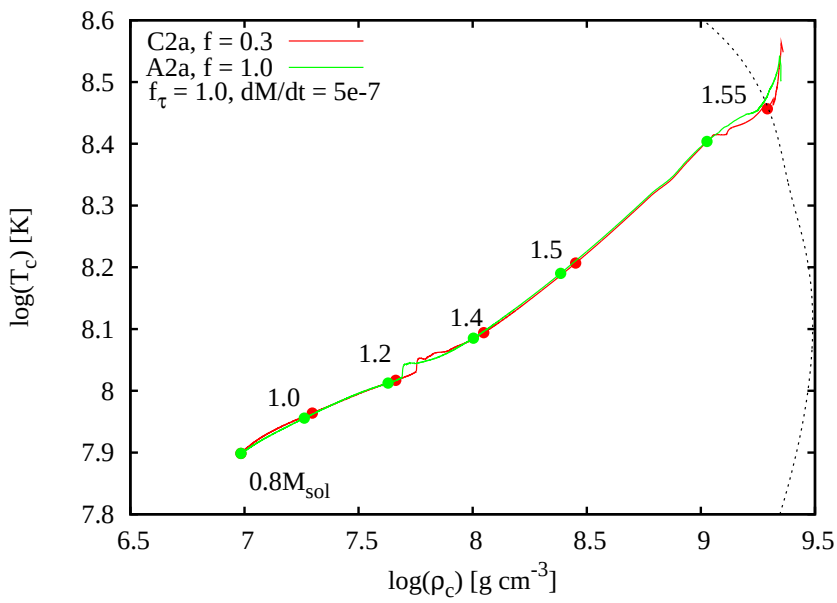

Figure 27: Evolutionary tracks in the central density and temperature plane for two sequences with different angular momentum gain factors f. The numbers near the dots denote the white dwarf masses in solar masses.

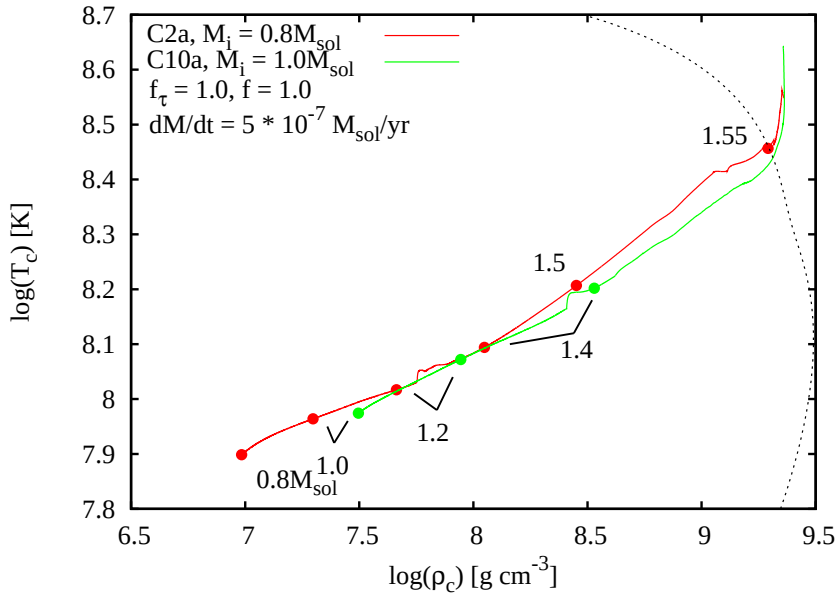

Figure 28: Evolutionary tracks in the central density and temperature plane for two sequences with different initial masses.

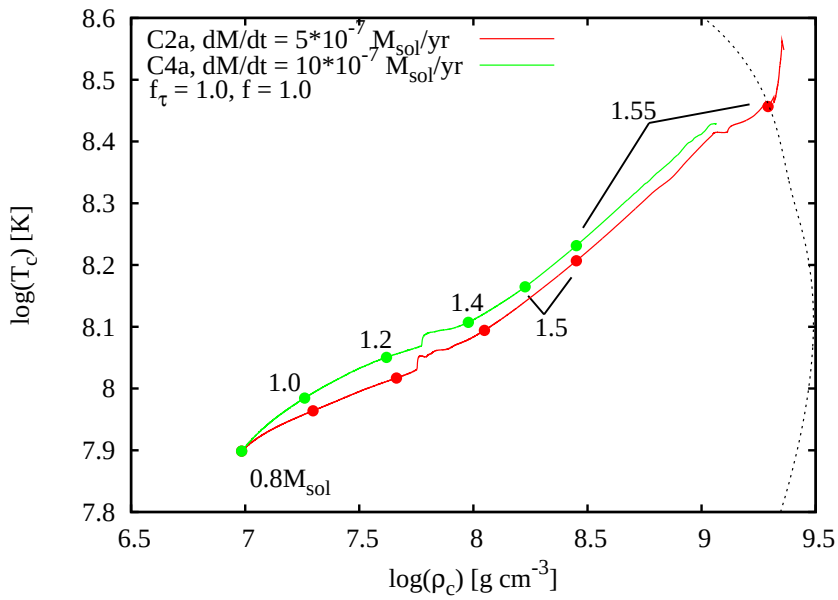

Figure 29: Evolutionary tracks in the central density and temperature plane for two sequences with different mass accretion rates.

5 Discussion

In Sect. 4.1 (Fig. 7) it has been shown that the ignition density of angular momentum losing super-Chandrasekhar-mass white dwarfs depends on the strength of the gravitational radiation, and thus the angular-momentum-loss timescale. This is demonstrated in Fig. 30, which shows the ignition density as function of the time delay between the end of the accretion and central carbon ignition, for our sequences assuming angular momentum loss only after the accretion phase ended. Iwamoto et al. (1999) have found constraints for the central ignition density for Type Ia supernovae, based on calculations of chemical yields for different central ignition densities. According to their results the central density of an "average" Type Ia supernova progenitor has to be $\leq 2 \cdot 10^9\,\mathrm{g\,cm^{-3}}$ to avoid excessively large ratios of $^{54}\mathrm{Cr}/^{56}\mathrm{Fe}$. If we compare this constraint to the results of the sequences with different but constant angular-momentum-loss timescales, we find that the timescale should be short, with $f_\tau = 1.0$ being a plausible value. It should be noted that the results of Iwamoto et al. were derived using only Chandrasekhar-mass progenitors.

Our sequences with angular momentum loss due to gravitational radiation after the accretion phase show that white dwarfs of different masses with a given strength of the r-mode oscillation, i.e. $f\tau = 1.0$, tend to avoid ignition at central temperatures lower than $2{\cdot}10^8$ K (Fig. 19). This limits the central densities at which white dwarfs of masses between 1.42 and $1.70\,M_\odot$ cross the carbon-ignition line to $1.7 \cdot 10^9\,\mathrm{g\,cm^{-3}} < \rho_{\mathrm{c,ign1}} < 2.3 \cdot 10^9\,\mathrm{g\,cm^{-3}}$.

If we plot the ignition masses against the ignition density we get Fig. 31. Again we see that only a few models ignite with central densities above $2.3 \cdot 10^9\,\mathrm{g\,cm^{-3}}$. The sequences with angular momentum loss due to gravitational radiation all had $f\tau = 1.0$. We know from the results from Sect. 4.1 that changing the angular-momentum-loss timescale leads to other ignition densities. But if $f\tau = 1.0$ indeed is a plausible value for the angular-momentum-loss timescale models we obtain ignition densities for sequences with angular momentum loss either during or after the accretion phase at the demanded value for the right chemical yields for most of our sequences.

Our simulations in Sect. 4.3 show that super-Chandrasekhar-mass white dwarfs still form when angular momentum is taken away by gravitational radiation during the accretion phase, even if the strength of the radiation effect is taken at the high end of the uncertainty range. This important result is found to be largely independent of the initial white dwarf mass, the mass accretion rate, the angular momentum accretion efficiency and the angular momentum loss timescale.

Our results show that the white dwarfs are not rotating rigidly at the time of carbon ignition, which might have significance for the propagation of the deflagration front during the explosion. However, an analysis of this is beyond the scope of this thesis. However, the angular velocity profiles

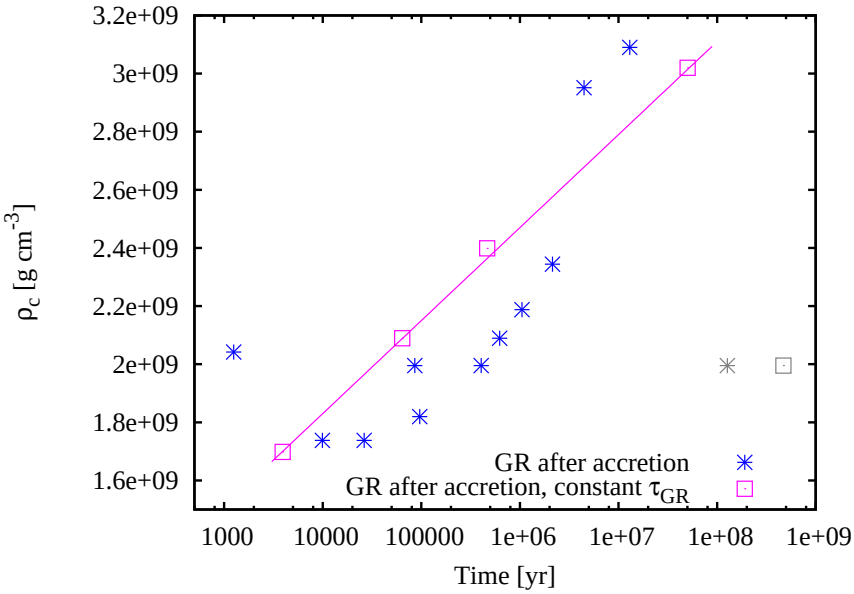

Figure 30: Central ignition density ($\rho_{\rm ign,1}$; cf. Tables 1 and 2) as function of the time between the onset of gravitational radiation and the ignition. The gray points are peculiar, these sequences cross the carbon-ignition line below the bend and may ignite at a higher central density, or not at all.

in our pre-supernova models vary, and it is interesting to see if this has an effect on the rotational energy and angular momentum of these models. Fig. 32 shows the rotational energy at ignition time as a function of mass, for sequences with different types of evolution. It appears that the differences in the degree of differential rotation are small enough to confine all sequences to a line in the ignition mass and rotational energy plane. It does not matter if angular momentum is taken during or after the accretion phase, or not at all. The timescale of angular momentum loss also has only a small effect on the rotational energy at ignition.

Fig. 33 shows that the same clustering to one line is present in the ignition mass and angular momentum plane.

The kinetic energy released by a Type Ia supernovae roughly equals the energy released by carbon and oxygen burning, minus the binding energy of the progenitor. Figs. 34 and 35 show this binding energy and the binding energy per solar mass as function of the ignition mass, respectively.

Perhaps the variance in peak luminosity and luminosity decline rate of Type Ia supernovae can be explained by one parameter only, as models with equal ignition mass are all very similar, even though their pre-supernova evolution can be very different. They may ignite while still in the accretion phase or $> 10^6$ yr after the accretion has ended and still show relatively

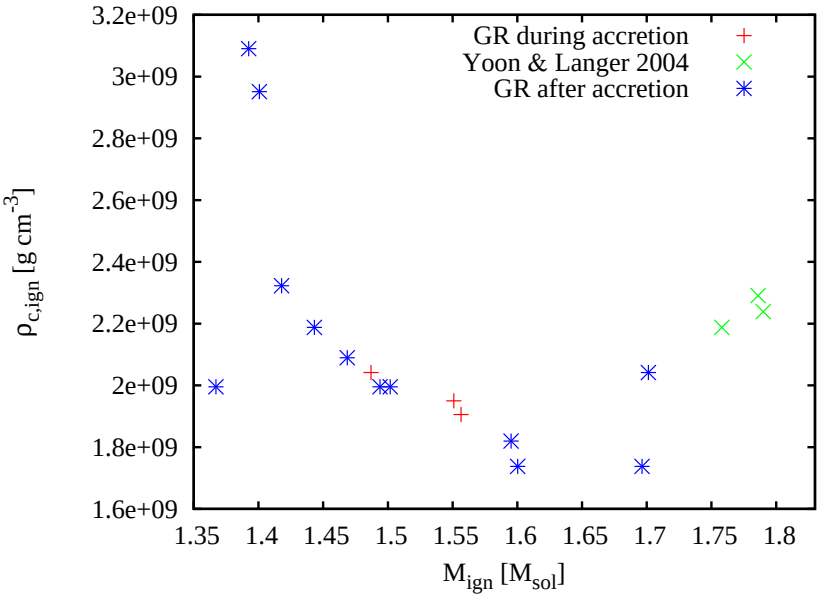

Figure 31: Central ignition density as function of the ignition mass for sequences with $\tau_{\rm GR} = 1.0$. The model with $M = 1.37\,{\rm M}_\odot$ may not ignite at the indicated density by at a density of $\simeq 3 \cdot 10^9$ g cm^{-3} when it follows the carbon-ignition line up to the turning point.

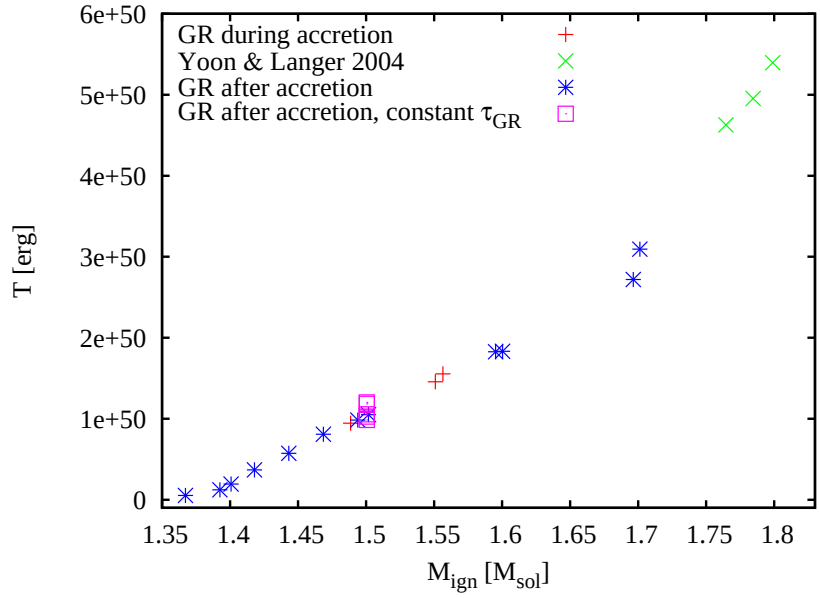

Figure 32: Rotational energy as function of the ignition mass.

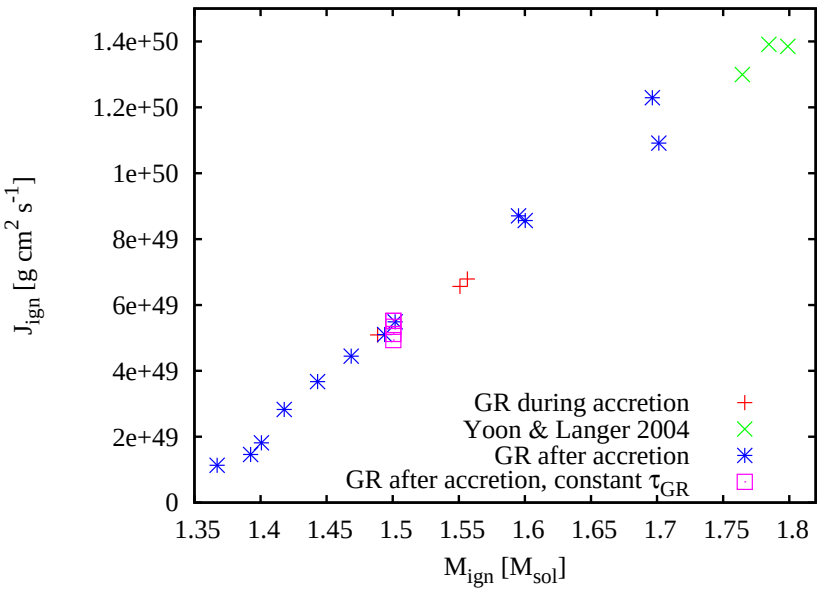

Figure 33: Angular momentum as function of the ignition mass.

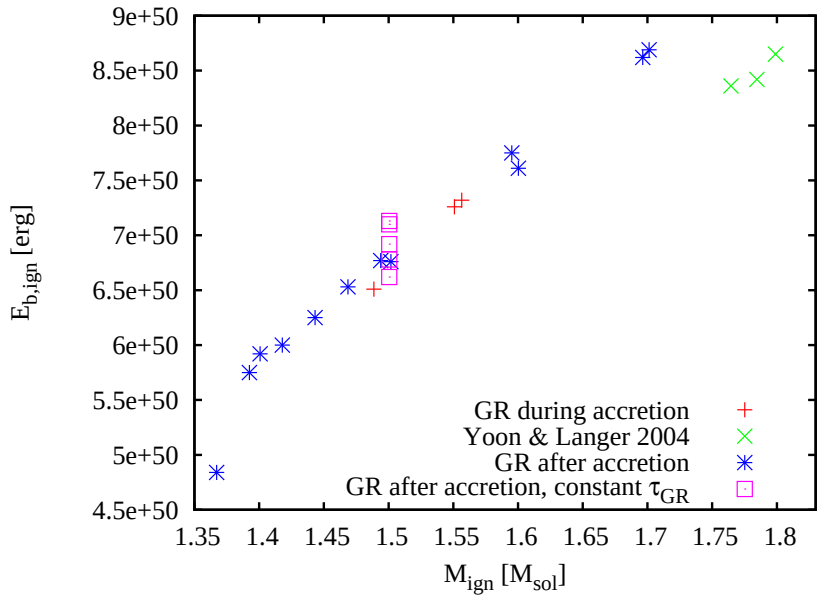

Figure 34: Binding energy as function of the ignition mass.

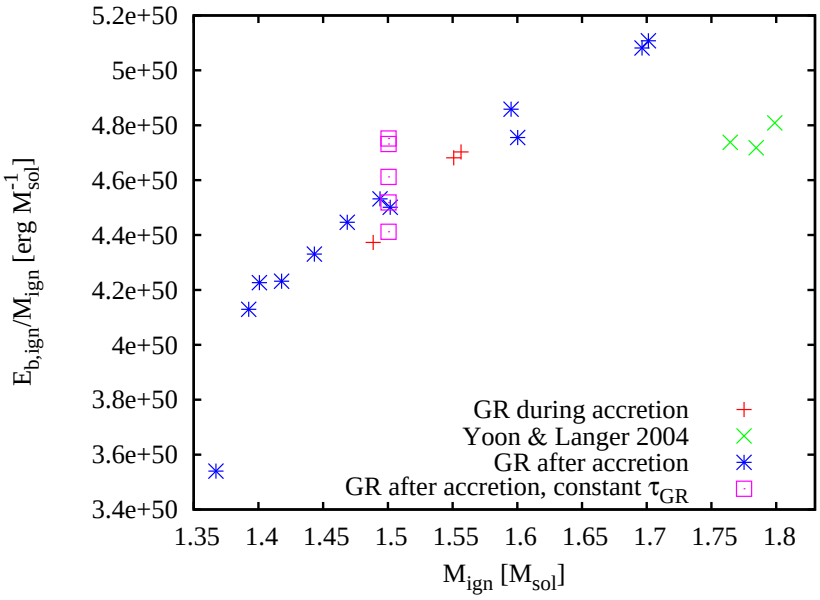

Figure 35: Binding energy per solar mass as function of the ignition mass. The energy released by burning $0.5\,\mathrm{M}_\odot$ of carbon and $0.5\,\mathrm{M}_\odot$ of oxygen completely to nickel is $1.56 \cdot 10^{51}$ erg.

little difference in the rotational and binding energy at the onset of carbon ignition.

The energy source of the expanding supernova is the decay of ^{56}Ni. This process gives gamma rays that scatter within the ejecta and become optical photons. The luminosity decay time depends mainly on the effective diffusion time $\tau_m \propto (\kappa M/v_{\rm exp} c)^{1/2}$ where κ is the opacity, c the speeds of light and $v_{\rm exp} \propto (E_{\rm kin}/M)^{1/2}$ with $E_{\rm kin}$ the kinetic energy of the explosion. Typical values for the kinetic energy are about $E_{\rm kin} = 1.3 \pm 0.1 \cdot 10^{51}$ erg for Chandrasekhar-mass progenitors (Nomoto et al., 1997).

If we assume that the fraction of white dwarf mass converted into ^{56}Ni is equal for all progenitor masses, than the amount of ^{56}Ni produced during the explosion is proportional to the progenitor mass. In this case, the supernova luminosity would increase with progenitor mass. Higher progenitor masses will also affect the luminosity decay time because more ^{56}Ni means more heating of the surface layer, thus raising κ. A higher progenitor mass also gives lower ejecta velocities because the binding energy per unit mass is higher and thus, per unit mass, less explosion energy can go into kinetic energy (Fig. 35). Raising κ and lowering $v_{\rm exp}$ raises the diffusion time and thus the luminosity decay time. Such a scenario might therefore explain the relation between the peak brightness and the luminosity decay rate. However, our we have to await realistic super-Chandrasekhar-mass explosion

models to see whether indeed more nickel is produced at higher mass, and whether quantitatively the mentioned effects are sufficient to explain the observed spread in absolute peak luminosities and luminosity decay rates (cf. Fig. 1).

6 Type Ia supernova's als hectometerpaaltjes

Figure 36: Voorbeeld van een Type Ia supernova, aangegeven met het pijltje. Deze supernova, SN2002bo, vond plaats op een afstand van ongeveer 30 miljoen lichtjaar en was tijdelijk net zo helder als alle andere sterren in het sterrenstelsel samen.

Een supernova van het type Ia is een sterexplosie die zo krachtig is dat ze voor enkele dagen helderder is dan een heel sterrenstelsel, een voorbeeld is te zien in Fig. 36. Door deze grote helderheid zijn ze tot aan de grenzen van het Heelal waar te nemen. Uit waarnemingen blijkt dat we de intrinsieke helderheid kunnen bepalen door de uitdooftijd te meten (zie Fig.1). Door deze relatie te ijken voor nabije supernova's is het een koud kunstje om uit de waargenomen helderheid en uitdooftijd van verder weg gelegen supernova's de afstand te bepalen. Daarom kunnen Type Ia supernova's gebruikt worden als 'hectometerpaaltjes', of *standard candles*, om de geometrie van het heelal te bepalen. Hoewel, eigenlijk weten we niet zeker hoe sterk deze relatie op zeer grote afstanden (en dus ver terug in de tijd) nog blijft gelden. Dat komt omdat de oorzaak van Type Ia supernova's nog maar gedeeltelijk verklaard is. We weten alleen zeker dat het nucleaire explosies van witte dwergen zijn.

Voor mijn afstudeeronderzoek heb ik samen met Norbert Langer en Sung-Chul Yoon geprobeert om met behulp van computersimulaties meer zekerheid omtrend het supernovascenario te verkrijgen.

Witte dwergen zijn het eindproduct van zeer veel hoofdreekssterren en

dientengevolge zijn ze er in soorten en maten. De witte dwergen die nodig zijn om Type Ia supernova's te verklaren zijn eigenlijk de naakte kernen van sterren die heliumfusie hebben doorgemaakt en daarna hun waterstofrijke buitenlagen afgestoten hebben. Deze kern bestaat uit de restproducten van heliumfusie, voornamenlijk koolstof en zuurstof. De massa varieert een beetje, maar is vergelijkbaar met de massa van de zon. Zouden deze witte dwergen geïsoleerd zijn dan zouden ze enkel afkoelen, maar velen worden gevormd in dubbelsterren en ondergaan interessantere veranderingen. Als de begeleider minder ver ontwikkeld is kan er overdracht van waterstof of helium van de begeleider naar de witte dwerg plaatsvinden, zodat de witte dwerg zwaarder wordt (zie Fig 2).

Hoewel de massa vergelijkbaar is met die van de zon, is het formaat van witte dwergen veel kleiner. Hun diameter is minder dan 1% van de diameter van de zon. Het gas in witte dwergen is daarom zo dicht opeengepakt dat het gedegenereert raakt, met als gevolg dat de druk die witte dwergen ervan weerhoud om onder invloed van hun eigen zwaartekracht ineen te storten alleen afhankelijk is van de dichtheid van het gas en niet van de temperatuur. Dit leidt er weer toe dat witte dweren kleiner worden als ze zwaarder worden om genoeg interne druk op te bouwen en dus is de dichtheid van zwaardere witte dwergen hoger dan die van lichtere witte dwergen. Als de dichtheid genoeg stijgt kan het koolstof in de kern van de witte dwerg langzaam fuseren tot zwaardere elementen. De door fusie gegenereerde energie kan dan nog met neutrino's afgevoerd worden en er treedt geen kettingreactie op. Maar als de dichtheid boven een bepaalde critische dichtheid komt, de ontstekingsdichtheid, kan de energie niet meer met neutrino's afgevoerd worden en zal het smeulen overgaan in een thermonucleaire explosie. Omdat de witte dwerg in eerste instantie niet uitzet tijdens de explosieve verbranding, kan in korte tijd bijna al het koolstof en zuurtstof omgezet worden in o.a. nikkel. De hoeveelheid energie die hierbij vrijkomt is meer dan genoeg om uiteindelijk de hele witte dwerg te vernietigen. De massa waarbij dit voor niet-roterende witte dwergen gebeurt is ongeveer 1.38 maal de massa van de zon (die hierna afgekort wordt tot $M_\odot$). Dit scenario is de meest geaccepteerde beschrijving van Type Ia supernova's, maar ze heeft nog een groot probleem. Waarnemingen wijzen uit dat er een zekere spreiding in de intrinsieke helderheid van de explosies zit, terwijl witte dwergen volgens bovenstaand scenario's net voor de explosie vrijwel identiek zijn. Verklaringen voor deze spreiding zijn gezocht in verschillen in de verhouding koolstof-zuurstof en in de vervuilingsgraad met elementen zwaarder dan zuurstof, maar dit wordt weersproken door computermodellen.

Deze computermodellen ginger er echter altijd vanuit dat dit supernovascenario altijd tot explosies bij $1.38\,M_\odot$ leidde, maar dit is afhankelijk van de rotatiesnelheid van de ster. Als een witte dwerg roteert zal door de centrifugale kracht de dichtheid kleiner zijn dan als hij stil staat. Daarom zal de critische dichtheid ook pas bij een hogere massa bereikt worden, afhankelijk

van de draaisnelheid. De massaoverdracht naar witte dwergen verloopt via een accretieschijf waarin het gas eerst rond de dwerg cirkelt voordat het uiteindelijk op het oppervlak terecht komt. Als het dan op het oppervlak valt zal het de witte dwerg een zetje geven zodat deze steeds sneller zal gaan draaien. Voorheen werd dit effect altijd verwaarloosd, maar Sung-Chul Yoon en Norbert Langer van het Sterrekundig Instituut Utrecht hebben met evolutiemodellen waarin dit rotatieëffect wel werd meegenomen, aangetoond dat koolstof-zuurstof witte dwergen gedurende de accretiefase kunnen groeien tot $\sim 1.9\,\mathrm{M}_\odot$, zonder de critische dichtheid te bereiken.

Om deze witte dwergen te laten exploderen moet er een mechanisme zijn dat de rotatie weer doet afnemen tot de critische dichtheid bereikt is. Dit hebben we gevonden in het uitzenden van gravitatiestraling. Roterende witte dwergen zijn gevoelig voor allerlei soorten verstoringen, waaronder de zogenaamde r-mode oscillatie. Deze oscillatie is het gevolg van de door rotatie veroorzaakte Coriolis-kracht en is zichtbaar als een paar wervelingen die over de ster trekken, zie Fig. 5. Deze wervelingen breken de rotatiesymmetrie van de ster en zenden gravitatiestraling uit, die naast energie ook impulsmoment (=een maat voor rotatie) van de ster wegneemt. Voor een waarnemer die niet met de ster meedraait lijkt dit patroon van wervelingen langzamer te draaien dan de ster zelf, om precies te zijn met precies 2/3 van de rotatiesnelheid van de ster. De hoeveelheid impulsmoment van een ster kan gezien worden als de som van het impulsmoment van de onverstoorde toestand en het impulsmoment van de verstoring (in dit geval de r-mode oscillatie). Doordat de verstoring gravitatiegolven uitzendt neemt zijn impulsmoment af, maar doordat de rotatiesnelheid van de verstoring gekoppeld is aan de rotatiesnelheid van de onverstoorde toestand, kan dat in eerste instantie alleen door de amplitude van de verstoring te laten toenemen. Dit heeft als gevolg dat de verstoring nog meer gravitatiegolven uitzendt en zou in principe ongelimiteerde groei van de verstoring betekenen, ware het niet dat er een verzadigingsamplitude is, veroorzaakt door de stroperigheid van de ster. Als de verzadigingsamplitude bereikt is, komt het weggestraalde impulsmoment niet meer uit de verstoring, maar uit de rotatie van de ster als geheel, die als gevolg hiervan afremt. Dit effect is al bestudeerd door anderen, maar alleen voor witte dwergen van $1.38\,\mathrm{M}_\odot$, die ook nog eens roteerde als starre lichamen. Wij hebben wel gekeken naar de effecten van differentiele rotatie, waarbij de verschillende lagen van de ster niet even snel hoefden te roteren en natuurlijk naar witte dwergen van verschillende massa's.

Het verlies van impulsmoment (J) gedurende een bepaalde periode (Δt) kan benaderd worden met

$$\Delta J(t) = J(t) * (1 - e^{-\Delta t/\tau_{\mathrm{GR}}})$$

waarbij τ_{GR} de tijdschaal is waarop het impulsmoment afneemt. We hebben de geavanceerdheid van ons model in stappen opgeschroeft. Eerst hebben

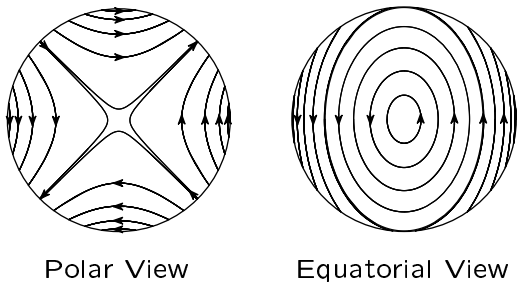

Figure 37: Patroon van de r-mode oscillatie op een ster. Voor een stilstaande waarnemer draait dit patroon langzamer dan de ster als geheel.

we aangenomen dat τ_{GR} een constante waarde heeft. Daarna hebben we een theoretische benadering voor τ_{GR} gebruikt, die we aangepast hebben om de effecten van differentiële rotatie weer te geven; met als startmodellen witte dwergen van verschillende massa's en met verschillende rotatiesnelheden. En als laatste hebben we berekend wat er zou gebeuren als de gravitatiestraling reeds tijdens de massaoverdrachtsfase uitgezonden wordt. Hierbij hebben we steeds een sterevolutie programma gebruikt waar binnen het Sterrekundig Instituut al veel ervaring mee is opgedaan. Hoewel het een één dimensionale benadering is, kan deze goed de evolutie van roterende sterren doorrekenen vanaf hun geboorte totaan hun dood.

De sterkte van de gravitatiestraling is niet precies bekend. We hebben daarom gekeken wat de verschillen in uitkomst zijn voor verschillende, constante, waarden voor τ_{GR}. Uit deze eerste reeks berekeningen bleek dat witte dwergen die hun impulsmoment sneller verliezen, bij een hogere temperatuur exploderen. Dit kan makkelijk verklaard worden doordat gas dat samengedrukt wordt opwarmt en sterren die sneller samen gedrukt worden die extra warmte niet kwijt kunnen raken. Deze hogere temperatuur zorgt voor een iets lagere critische dichtheid, wat gevolgen heeft voor de chemische samenstelling van de 'asresten' van de explosie. Met deze resultaten konden we ook verifiëren dat de in de literatuur gevonden orde grootte voor τ_{GR} redelijk betrouwbaar was. Voor een witte dwerg van $1.5\,\mathrm{M}_\odot$ is dat enkele honderdduizenden jaren.

Voor de tweede en derde reeks berekingen hebben we de constante waarde voor τ_{GR} vervangen door

$$\tau_{\mathrm{GR},i} = \frac{4\pi j_i}{J A r_i^4 \omega_i^6}$$

met j_i het specifieke impulsmoment van een laag binnenin de witte dwerg, ω_i en r_i respectievelijk de hoeksnelheid en straal van deze laag, J het totale impulsmoment van de ster en A een constante. Als de ster langzamer roteert neemt $\tau_{\mathrm{GR},i}$ toe en het zou dus mogelijk zijn dat de ster nooit genoeg afremt

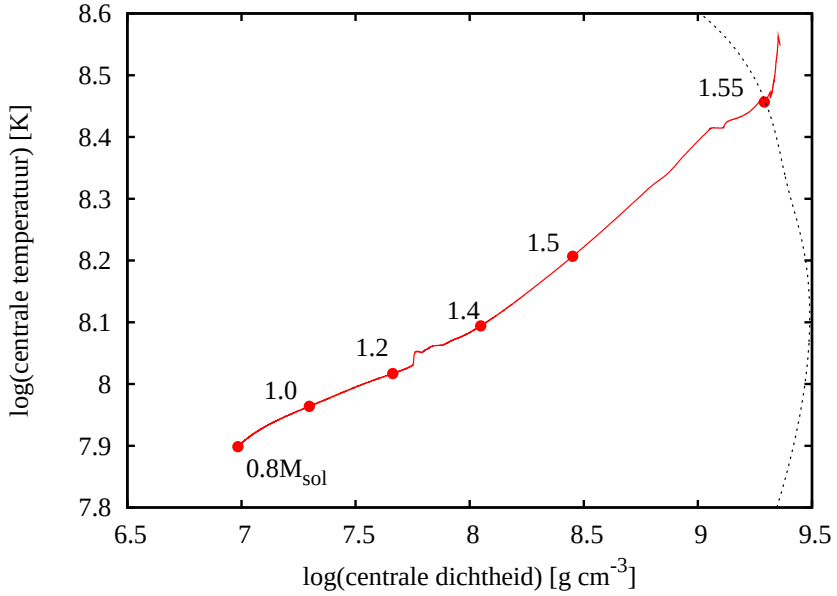

Figure 38: Voorbeeld van een witte dwerg met massa toename. De toename was hier $5 \cdot 10^{-7}\,\mathrm{M}_\odot/\mathrm{yr}$.

om te exploderen omdat de afremming steeds minder snel gaat. Dit bleek echter niet zo te zijn. Alle witte dwergen boven $1.38\,\mathrm{M}_\odot$ remde snel genoeg af om te exploderen na een periode van afremming die aanzienlijk korter is dan de leeftijd van het Heelal.

Uit de derde reeks berekeningen bleek dat ook witte dwergen die door het uitzenden van gravitatiestraling minder snel opspinnen tijdens de massaoverdrachtsfase, toch zwaarder dan $1.38\,\mathrm{M}_\odot$ kunnen worden. Aangezien de r-mode oscillaties in hun groei beperkt worden door wervelingen veroorzaakt door de massaoverdracht, is dit een versterking van de conclusie dat witte dwergen zwaarder dan $1.38\,\mathrm{M}_\odot$ kunnen worden en niet allemaal bij dezelfde massa zullen exploderen. Fig. 38 geeft een voorbeeld van hoe de ster verandert met toenemende massa. Naarmate de ster zwaarder wordt neemt de centrale dichtheid toe, totdat deze uiteindelijk een critische grens overschrijdt (aangegeven met de zwarte stippellijn) en de ster explodeert (in dit figuur te zien door de scherpe stijging in temperatuur aan het einde van de lijn).

Uit onze resultaten kunnen we twee conclusies trekken. Ten eerste dat er een bereik van massa's van witte dwergen is, dat als Type Ia supernova zal eindigen. Wellicht is dit meteen de verklaring voor de waargenomen spreiding in intrinsieke helderheid, zwaardere witte dwergen hebben immers meer koolstof en zuurstof om te fuseren. De tweede betrof de homogeniteit van de witte dwergen vlak voor de explosie. Het bleek dat de hoeveelheid impulsmo-

ment op het moment van het begin van de explosie alleen afhankelijk was van de massa, terwijl wij zo'n nauwe relatie niet verwachtten daar de witte dwergen verschillende soorten evolutie hebben doorgemaakt. Het resultaat van deze homogeniteit is dat zwaardere witte dwergen bijna zonder uitzondering een hogere bindingsenergie per massaeenheid hebben dan lichtere. Misschien kan dit de relatie tussen de maximale helderheid en de uitdooftijd verklaren. Een hogere bindingsenergie per massaeenheid betekend dat de uitdijende resten van de explosie een lagere snelheid zullen hebben, en dus dat de vuurbal minder snel oplost.

Het antwoord op deze vragen komt hopenlijk snel. Binnenkort zullen onze pre-supernova modellen door onderzoekers van het Max Planck instituut in Duitsland gebruikt worden als startmodellen voor onderzoek naar de uiteindelijke explosie. Daar gebruiken ze meer-dimensionale computermodellen die de explosie zelf kunnen doorrekenen.

References

Anand, S. P. S.: 1968, *ApJ* **153**, 135

Andersson, N.: 1998, *ApJ* **502**, 708

Andersson, N. and Kokkotas, K.: 2001, *International Journal of Modern Physics D* **10**, 381

Arras, P., Flanagan, E. E., Morsink, S. M., Schenk, A. K., Teukolsky, S. A., and Wasserman, I.: 2003, *ApJ* **591**, 1129

Bennett, C. L., Halpern, M., Hinshaw, G., Jarosik, N., Kogut, A., Limon, M., Meyer, S. S., Page, L., Spergel, D. N., Tucker, G. S., Wollack, E., Wright, E. L., Barnes, C., Greason, M. R., Hill, R. S., Komatsu, E., Nolta, M. R., Odegard, N., Peiris, H. V., Verde, L., and Weiland, J. L.: 2003, *ApJ Supplement* **148**, 1

Branch, D., Fisher, A., and Nugent, P.: 1993, *The Astronomical Journal* **106**, 2383

Canuto, V.: 1970, *ApJ* **159**, 641

Chandrasekhar, S.: 1970, *ApJ* **161**, 561

Durisen, R.: 1975, *ApJ* **199**, 179

Durisen, R. H.: 1977, *ApJ* **213**, 145

Endal, A. S. and Sofia, S.: 1976, *ApJ* **210**, 184

Friedman, J. L. and Morsink, S. M.: 1998, *ApJ* **502**, 714

Friedman, J. L. and Schutz, B. F.: 1978, *ApJ* **222**, 281

Höflich, P., Khokhlov, A., Wheeler, J. C., Phillips, M. M., Suntzeff, N. B., and Hamuy, M.: 1996, *ApJ Letters* **472**, L81

Höflich, P., Wheeler, J. C., and Thielemann, F. K.: 1998, *ApJ* **495**, 617

Hubbard, W. B. and Lampe, M.: 1969, *ApJ Supplement* **18**, 297

Ibanez-Cabanell, J. M.: 1983, *Revista Mexicana de Astronomia y Astrofisica* **8**, 7

Ichimaru, S. and Ogata, S.: 1991, *ApJ* **374**, 647

Iglesias, C. A. and Rogers, F. J.: 1996, *ApJ* **464**, 943

Iwamoto, K., Brachwitz, F., Nomoto, K., Kishimoto, N., Umeda, H., Hix, W. R., and Thielemann, F.: 1999, *ApJ Supplement* **125**, 439

Kippenhahn, R. and Möllenhoff, C.: 1974, *Astrophysics and Space Science* **31**, 117

Knop, R. A., Aldering, G., Amanullah, R., Astier, P., Blanc, G., Burns, M. S., Conley, A., Deustua, S. E., Doi, M., Ellis, R., Fabbro, S., Folatelli, G., Fruchter, A. S., Garavini, G., Garmond, S., Garton, K., Gibbons, R., Goldhaber, G., Goobar, A., Groom, D. E., Hardin, D., Hook, I., Howell, D. A., Kim, A. G., Lee, B. C., Lidman, C., Mendez, J., Nobili, S., Nugent, P. E., Pain, R., Panagia, N., Pennypacker, C. R., Perlmutter, S., Quimby, R., Raux, J., Regnault, N., Ruiz-Lapuente, P., Sainton, G., Schaefer, B., Schahmaneche, K., Smith, E., Spadafora, A. L., Stanishev, V., Sullivan, M., Walton, N. A., Wang, L., Wood-Vasey, W. M., and Yasuda, N.: 2003, *ApJ* **598**, 102

Langer, N., Deutschmann, A., Wellstein, S., and Höflich, P.: 2000, *A&A* **362**, 1046

Levin, Y. and Ushomirsky, G.: 2001, *MNRAS* **322**, 515

Lindblom, L., Owen, B. J., and Morsink, S. M.: 1998, *Phys. Rev. Letters* **80**, 4843

Lindblom, L., Tohline, J. E., and Vallisneri, M.: 2002, *Phys. Rev. D* **65(8)**, 084039

Livio, M.: 2000, in *Proceedings of The greatest Explosions since the Big Bang: Supernovae and Gamma-Ray Bursts, held 3-6 May, 1999 at Space Telescope Science Institute edited by Mario Livio, Nino Panagia and Kailash Sahu*

Neo, S., Miyaji, S., Nomoto, K., and Sugimoto, D.: 1977, *Publications of the Astronomical Society of Japan* **29**, 249

Nomoto, K., Iwamoto, K., and Kishimoto, N.: 1997, *Science* **276**, 1378

Paczyński, B.: 1991, *ApJ* **370**, 597

Perlmutter, S. and Schmidt, B. P.: 2003, *LNP: Supernovae and Gamma-Ray Bursters* **598**, 195

Phillips, M. M.: 1993, *ApJ Letters* **413**, L105

Popham, R. and Narayan, R.: 1991, *ApJ* **370**, 604

Röpke, F. K. and Hillebrandt, W.: 2004, *A&A* **420**, L1

Sahrling, M.: 1994, *A&A* **284**, 484

Saio, H. and Nomoto, K.: 1998, *ApJ* **500**, 388

Shapiro, S. L. and Teukolsky, S. A.: 1983, *Black holes, white dwarfs, and neutron stars: The physics of compact objects*, Wiley-Interscience, New York

Thorne, K. S.: 1980, *Reviews of Modern Physics* **52**, 299

Woosley, S. E., Taam, R. E., and Weaver, T. A.: 1986, *ApJ* **301**, 601

Yoon, S.-C. and Langer, N.: 2002, in *ASP Conf. Ser. 261: The Physics of Cataclysmic Variables and Related Objects*

Yoon, S. C. and Langer, N.: 2004, *A&A* **419**, 623

Zahn, J.-P.: 1992, *A&A* **265**, 115